Efficacy of early stellar feedback in low gas surface density environments

Rahul Kannan,[1]⋆† Federico Marinacci [ID],[1] Christine M. Simpson [ID],[2,3,4]
Simon C. O. Glover[5] and Lars Hernquist[1]

[1]*Harvard-Smithsonian Center for Astrophysics, 60 Garden Street, Cambridge 02138, MA, USA*
[2]*Heidelberg Institute for Theoretical Studies, Schloss- Wolfsbrunnenweg 35, D-69118 Heidelberg, Germany*
[3]*Enrico Fermi Institute, University of Chicago, Chicago, IL 60637, USA*
[4]*Department of Astronomy & Astrophysics, University of Chicago, Chicago, IL 60637, USA*
[5]*Universiät Heidelberg, Zentrum für Astronomie, Institut für theoretische Astrophysik, Albert-Ueberle-Str 2, D-69120 Heidelberg, Germany*

ABSTRACT

We present a suite of high-resolution radiation hydrodynamic simulations of a small patch $(1 \, \mathrm{kpc}^2)$ of the interstellar medium (ISM) performed with AREPO-RT, with the aim to quantify the efficacy of various feedback processes like supernova (SN) explosions, photoheating, and radiation pressure in low gas surface density galaxies ($\Sigma_{gas} \simeq 10 \, \mathrm{M}_\odot \, \mathrm{pc}^{-2}$). We show that radiative feedback decrease the star formation rate and therefore the total stellar mass formed by a factor of approximately two. This increases the gas depletion time-scale and brings the simulated Kennicutt–Schmidt relation closer to the observational estimates. Radiation feedback coupled with SN is more efficient at driving outflows with the mass and energy loading increasing by a factor of ~ 10. This increase is mainly driven by the additional entrainment of medium-density ($10^{-2} \, \mathrm{cm}^{-3} \leq n < 1 \, \mathrm{cm}^{-3}$) warm ($300 \, \mathrm{K} \leq T < 8000 \, \mathrm{K}$) material. Therefore, including radiative feedback tends to launch colder, denser, and more mass- and energy-loaded outflows. This is because photoheating of the high-density gas around a newly formed star overpressurizes the region, causing it to expand. This reduces the ambient density in which the SN explode by a factor of 10–100 which in turn increases their momentum output by a factor of $\sim$1.5–2.5. Finally, we note that in these low gas surface density environments, radiative feedback primarily impact the ISM via photoheating and radiation pressure has only a minimal role in regulating star formation.

Key words: radiative transfer – methods: numerical – ISM: structure – galaxies: ISM.

1 INTRODUCTION

Stellar feedback has been invoked by many models to explain the low efficiency of star formation in low-mass ($M_{halo} \lesssim 10^{12} \, \mathrm{M}_\odot$) haloes (Navarro, Frenk & White 1996; Springel & Hernquist 2003; Stinson et al. 2006; Dalla Vecchia & Schaye 2008; Agertz et al. 2013; Vogelsberger et al. 2013; Hopkins et al. 2014, 2017). Early cosmological simulations invoked the energy injection from supernova (SN) events as the main feedback mechanism to regulate star formation. However, the coupling between SN feedback energy and the interstellar medium (ISM) was seen to be very inefficient (Katz, Weinberg & Hernquist 1996; Navarro et al. 1996) due to the inability of the simulations to resolve the relevant scales. This precipitated the need to treat SN feedback on sub-grid scales, which involved models such as delayed cooling of gas heated by an SN

event (Thacker & Couchman 2001; Stinson et al. 2006; Agertz et al. 2013), stochastic heating of the gas to temperatures where cooling is inefficient (Dalla Vecchia & Schaye 2008; Schaye et al. 2015), and adding velocity kicks to gas particles to remove them from the inner regions of galactic discs (Springel & Hernquist 2003; Oppenheimer & Davé 2006; Vogelsberger et al. 2013). These models have been quite successful in reproducing a wide variety of galaxy properties (Kannan et al. 2014b; Vogelsberger et al. 2014a, b; Schaye et al. 2015; Davé, Thompson & Hopkins 2016; Dubois et al. 2016; Hopkins et al. 2018; Marinacci et al. 2018; Naiman et al. 2018; Nelson et al. 2018; Pillepich et al. 2018; Springel et al. 2018; Davé et al. 2019). However, they often require the tuning of free parameters that do not necessarily map to a set of physical processes. In many cases they also require unrealistically high values of SN feedback energy ($> 10^{51}$ erg; Guedes et al. 2011; Schaye et al. 2015) or unreasonably large outflow velocities (Pillepich et al. 2018).

Only recently has there been a push to quantify the momentum input of SN events by performing high-resolution simulations that resolve the cooling radius and the Sedov–Taylor (ST) phase of the

explosion (Blondin et al. 1998; Thornton et al. 1998; Kim & Ostriker 2015; Martizzi, Faucher-Giguère & Quataert 2015; Walch & Naab 2015; Haid et al. 2016), which showed that the amplification in momentum resulting from the ST expansion in the presence of cooling is of the order of ∼9–25. However, even with the momentum boost included, SN feedback alone is not able to regulate star formation in galaxies (Girichidis et al. 2016a), if the stars are assumed to form and explode in the high-density peaks of the ISM. Only for random SN positions is the energy injected in sufficiently low-density environments to reduce energy loses significantly. It enhances the effective coupling between the SN feedback energy and the ISM leading to more realistic velocity dispersions and strong, high mass-loaded winds leading to a global regulation of star formation. Similar results have been found by Simpson et al. (2016), who invoked cosmic ray pressure to drive large-scale outflows.

In addition to SN, massive young stars deposit substantial amounts of energy in the form of radiation and stellar winds (Leitherer et al. 1999; Murray, Quataert & Thompson 2010; Walch et al. 2012; Agertz et al. 2013). These high-energy photons ionize and photoheat the gas, driving small-scale winds and pre-processing the sites of SN explosions (Stinson et al. 2013). This aides in the regulation of star formation in galaxies, especially at high redshifts (Kannan et al. 2014b). However, this model assumes full thermalization of the injected UV radiation energy close to the source, which is not guaranteed as most of the energy of the photons is consumed to free the electron and it is only the remainder that goes into thermalizing the gas via the kinetic energy of the ejected electron. Single scattering UV and multiscattered infrared (IR) radiation pressure is another mechanism invoked to drive significant outflows (∼ 100 km s^{-1}) (Hopkins, Quataert & Murray 2011; Agertz et al. 2013; Hopkins et al. 2014). It is, however, unclear whether the the gas can actually trap the photons efficiently. Krumholz & Thompson (2013), using a flux-limited diffusion (FLD) RT scheme, showed that as the gas accelerates in the presence of the gravitational potential of the disc, it becomes Rayleigh–Taylor unstable, creating channels through which photons escape, reducing the efficacy of this mechanism. Simulations performed with more accurate RT algorithms disagree with the previous calculations and show that it is indeed possible to drive outflows even when the gas becomes Rayleigh–Taylor unstable (Davis et al. 2014; Zhang & Davis 2017). In any case, large optical depths ($\tau_{IR} \sim 50$) are required to effectively trap the photons and boost the momentum injection to the levels required to efficiently suppress star formation (Roškar et al. 2014). These conditions are currently thought to only exist in galaxies with extremely high gas surface densities $\Sigma_{gas} \gtrsim 200 \, M_\odot \, pc^{-2}$. Alternatively, the high-energy photons escaping the ISM of galaxies will reduce the cooling rate of the circumgalactic medium (CGM) which, in turn, reduces the inflow into the centres of galaxies (Cantalupo 2010; Gnedin & Hollon 2012; Kannan et al. 2014a, 2016).

The empirical nature of these sub-grid models makes it difficult to determine the significance of radiation feedback in regulating the star formation rate (SFR) of galaxies. Full radiation hydrodynamic (RHD) simulations are therefore necessary in order to achieve a fundamental understanding of stellar feedback (Rosdahl et al. 2015; Kim & Ostriker 2017; Peters et al. 2017; Emerick, Bryan & Mac Low 2018). Rosdahl et al. (2015) using RHD isolated disc simulations showed that photoheating suppresses star formation by making the disc smooth and thick and by preventing of the formation of dense clouds (rather than dispersing them). Radiation pressure (both UV and multiscattering IR) was shown to be unimportant. The need to simulate the entire disc necessitated relatively low

resolutions (∼ 20–30 pc), which meant that both the Strömgren radius around young massive stars and the ST phase of the SN explosion were only partially resolved. Peters et al. (2017) showed that radiative feedback in combination with stellar winds can regulate star formation in solar-neighbourhood-like environments. However, the effect of radiation pressure was left unexplored.

In this paper, we perform high-resolution ($\Delta x \sim 0.45$ pc ; $M_{gas} = 10 \, M_\odot$) simulations of a patch of the ISM to investigate and quantify the role of various stellar feedback processes like SN, photoheating, and radiation pressure (both UV and multiscattered IR) in low gas surface density galaxies. These high resolutions ensure that the relevant spatial and mass scales are sufficiently resolved, thereby providing an accurate picture of stellar feedback. The paper is structured as follows. In Section 2, we outline the simulations performed. Section 3 describes the results obtained. The interpretation of the results is presented in Section 4 and finally, we present our conclusions in Section 5.

2 METHODS

The simulations are performed with AREPO-RT (Kannan et al. 2018), an RHD extension to the moving mesh code AREPO (Springel 2010; Pakmor et al. 2016). The simulation set-up is similar to the one described in Simpson et al. (2016) which in turn in based on the set-up described in Creasey, Theuns & Bower (2013). It consists of a column of gas of dimensions $1 \times 1 \times 10$ kpc representing a small portion of a galactic disc. The initial gas density profile ($\rho_{gas, 0}$) is given by

$$\rho_{gas,0} = \frac{\Sigma_0}{2b_0} \, sech^2 \left(\frac{h}{b_0} \right) \, , \qquad (1)$$

where the gas surface density is set to $\Sigma_0 = 10 \, M_\odot \, pc^{-2}$, the scale height is $b_0 = 100$ pc, and the gas fraction is $f_g = 0.1$. The stellar density field depends on the initial gas density field and the gas fraction (f_g) and is given by $\rho_\star = \rho_{gas,0}(f_g^{-1} - 1)$. Note that the gas fraction is smaller than the fiducial value of the solar neighbourhood ($f_g \simeq 0.25$), and the inverse correlation between the stellar potential and the gas fraction means that our gravitational potential is a factor of 2.5 larger than solar neighbourhood conditions. This has important implications for the SFRs obtained in our simulations (see Section 3 for more details). We impose a minimum density threshold of $4 \times 10^{-19} \, cm^{-3}$. Periodic boundaries are imposed along the two short, x and y axes, and outflow boundaries along the long (z) axis. The gravitational forces are computed as a sum of self-gravity and an external potential mimicking the pre-existing stellar density field. An adaptive softening is used for gas cells with a minimum value of $\epsilon_{gas} = 0.165$ pc. The collisionless stellar particles have a fixed softening of $\epsilon_{star} = 0.165$ pc.

The central disc is resolved by 10^6 gas cells, concentrated in the mid-plane. The rest of the simulation volume is initially comprised of a Cartesian mesh with a cell length of 43.5 pc up to 1 kpc and of 90.9 pc beyond. The mesh is refined and de-refined, so as to maintain roughly constant cell mass of $10 \, M_\odot$. Moreover, the volumes are approximately limited between 0.1 and $7.19 \times 10^5 \, pc^3$ with a maximum volume ratio of eight between adjacent cells. An effective pressure floor equal to 4^2 times the Jeans pressure (Machacek, Bryan & Abel 2001) is imposed in order to keep the Jeans length resolved after gravitational collapse has reached the minimum allowed cell volume. The Jeans pressure (P_J) in turn is defined as

$$P_J = \frac{G(\Delta x_{min} \rho)^2}{\pi \gamma} \, , \qquad (2)$$

where G is the gravitational constant, ρ is the density of the gas cell, and $\Delta x_{\min}$ is the minimum allowed diameter of the cell.

The RHD module solves the moment-based radiative transfer equations using the M1 closure relation. This closure method is fully local in nature, such that the computational cost is independent of the number of sources and only depends on the number of resolution elements in the simulation. We use the chemistry and cooling network outlined in Smith et al. (2014) . It solves the hydrogen chemistry, including H_2 (Glover & Mac Low 2007a, b) and has a simple treatment for CO chemistry (Nelson & Langer 1997; Glover & Clark 2012). The dust-to-gas ratio is assumed to be $f_d = 0.01$. We do not use any external radiation field as they will be generated self-consistently in our simulations. The chemistry network is coupled to stellar radiation using a multifrequency approach. We use six frequency bins: the IR band (0.1–1 eV), optical band (1–11.2 eV), the Lyman–Werner (LW; H_2 dissociation) band (11.2–13.6 eV), hydrogen ionization band (13.6–15.2 eV), H and H_2 ionization band (15.2–24.6 eV), and finally the He ionization band (24.6–100.0 eV). The dust opacity to IR radiation is set to $\kappa_{IR} = 10\,\mathrm{cm^2 g^{-1}}$ and the opacity for all other radiation bins is $\kappa_{UV} = 1000\,\mathrm{cm^2 g^{-1}}$. The photoionization and photoheating rates for each bin are calculated as described in section 3.2.1 of Kannan et al. (2018).

Accurately simulating H_2 thermochemistry is quite tricky as only about 10 per cent of the absorbed Lyman–Werner photons leads to dissociation (Draine & Bertoldi 1996; Sternberg et al. 2014). This effect is usually modelled using a self-shielding prescription that is dependent on the column density of H_2 (Gnedin & Draine 2014). Unfortunately, our formulation of the RT equations does not track the optical depth of individual rays. Therefore, we resort to using the method described in Nickerson, Teyssier & Rosdahl (2018) and boost the destruction of LW photons by a constant factor to mimic the inefficiency of LW photons in dissociating H_2. A test for this scheme is presented in Appendix A.

Stars are formed following a standard stochastic approach. The density threshold for star formation is set to $n = 100\,\mathrm{cm^{-3}}$. The SFR of a cell 'i' above this threshold is set to

$$\mathrm{sfr}_i = \epsilon_{\mathrm{ff}} \frac{m_i}{t_{\mathrm{ff}}} \,, \tag{3}$$

where m_i is the mass of the cell, ϵ_{ff} is the star formation efficiency per free-fall time of gas (set to 0.02), and t_{ff} is the free-fall time of the gas defined as

$$t_{\mathrm{ff}} = \sqrt{\frac{3\pi}{32 G \rho_i}} \,, \tag{4}$$

where ρ_i is the density of the cell. The probability of a cell forming a star is then given by

$$p_i = \mathrm{sfr}_i \frac{\Delta t}{m_\star} \,, \quad \text{where } m_\star = \min\{m_i, m_{\max}\} \,, \tag{5}$$

where Δt is the time-step of the gas particle. Collisionless particles of mass $m_\star$, representing stellar populations, are formed stochastically from the gas, with the probability of forming one drawn from a Poisson distribution. Note that if $m_i = m_\star$, then the whole cell is converted to stars else part of the cell mass is converted into stars with the maximum stellar mass set to $m_{\max} = 20\,\mathrm{M_\odot}$.

We assume a Chabrier (Chabrier 2003) stellar initial mass function (IMF). Stars with initial mass $M_\star \geq 8\,\mathrm{M_\odot}$ are assumed to explode as SN at the end of their lifetime. This sets the SN rate SNR ~ 1 per $100\,\mathrm{M_\odot}$ of stars formed. The extremely high-mass resolution of our simulations necessitates the need for a probabilistic

approach to stellar feedback. As soon as a star is formed, we tag that stellar particle to go SN in a probabilistic manner. The probability of a star going SN is given as

$$p_{\mathrm{SN}} = \mathrm{SNR} \frac{m_\star}{100\,\mathrm{M_\odot}} \,. \tag{6}$$

We then enforce that only the tagged SN particles emit radiation. This ensures that irrespective of the mass of the stellar particle, it emits radiation equivalent to $100\,\mathrm{M_\odot}$ of new stars formed. The radiation luminosity and spectra are obtained from Bruzual & Charlot (2003). The time delay between star formation and the SN event is set to 5 Myr. We assume that the stars only emit radiation during this time and as soon as they go SN their radiation output stops. This is a good approximation as stellar population synthesis models predict a precipitous drop in the radiation output after about 3 Myr, when the most massive stars start to die off. SN are modelled as discrete explosions of 10^{51} erg deposited as purely thermal energy into the 32 closest cells in a volume-weighted fashion. Explosion events are only added to the mesh when all gas cells are synchronized; the maximum allowed time-step is 0.1 Myr. The high mass and spatial resolution of our simulations ensures that the right momentum boost is recovered (Simpson et al. 2015, 2016).

The amount of UV ionizing photons per $100\,\mathrm{M_\odot}$ of stars formed is about $\dot{N}_\gamma = 5 \times 10^{48}$ photons s^{-1} (Bruzual & Charlot 2003). The Strömgren radius (r_s), assuming full ionization within r_s, is given by

$$r_s = 2.5\,\mathrm{pc} \left(\frac{\dot{N}_\gamma}{5 \times 10^{48}\,\mathrm{s^{-1}}} \right)^{1/3} \left(\frac{n_H}{100\,\mathrm{cm^{-3}}} \right)^{-2/3} \,, \tag{7}$$

where n_H is the hydrogen number density of gas. The minimum cell sizes in our simulation reaches about $0.1\,\mathrm{pc^3}$ which equates to maximum density at which the Strömgren radius is resolvable to $n = 2.6 \times 10^3\,\mathrm{cm^{-3}}$. Above this density r_s will be unresolved and the effect of photoheating will be underestimated. To increase the probability of resolving the r_s, we inject all the photons into the cell closest to the star particle. Additionally, the direction of the photon flux $(\mathbf{F}_r)$ is set to be radially outwards from the star particle and the magnitude is $|\mathbf{F}_r| = \tilde{c} E_r$, where E_r is the photon energy density and $\tilde{c}$ is the reduced speed of light, which in our simulations is set to $10^3\,\mathrm{km\,s^{-1}}$. This overcomes the issues mentioned in Hopkins & Grudic (2018) by ensuring that the full radiation pressure force is accounted for even if the cell optical depth is larger than one. However, this leads to anisotropic pressure forces around a star particle, but this is mitigated by the fact that we form a large number of stars during the simulation and each random orientation adds up to create an isotropic pressure force.

We perform four different simulations: SN: only the SN feedback is active; PH: SN + photoheating from UV sources is active; RP: PH + radiation pressure from just single scattering UV radiation is active, and finally IR: RP + effect of multiscattered IR radiation. Each of these simulations are run for $t = 150$ Myr. In this paper, we have decided to focus only on the effect of radiative feedback and hence our simulations neglect the effects of other important ingredients such as the magnetic field, winds from massive stars, and cosmic rays.

3 RESULTS

We begin by looking at the morphological evolution of the disc in our simulations. Fig. 1 shows the x–z (1×3 kpc) map of the column density integrated along the y-axis in the SN simulation at $t = 10$ (first column), 30 (second column), 50 (third column),
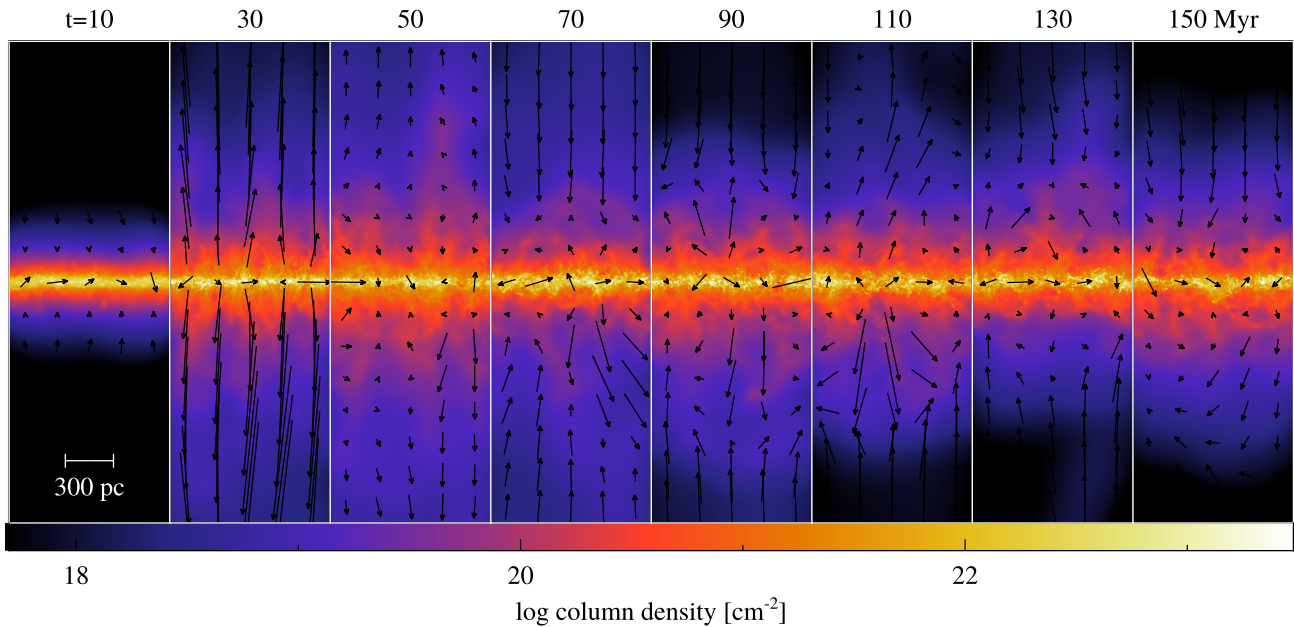
Figure 1. Map of the column density along the line of sight in the SN simulation at $t = 10$ (first column), 30 (second column), 50 (third column), 70 (fourth column), 90 (fifth column), 110 (sixth column), 130 (seventh column), and 150 (eighth column) Myr. The dimensions of the box shown in the image are 1×3 kpc. The black arrows indicate the direction of the velocity field with the length of the arrows indicating the magnitude of the mass-weighted velocity field. The initial starburst drives large-scale ($\sim$3–4 kpc) outflows ($t = 30$–50 Myr), followed by a period of infall ($t = 50$–70 Myr), after which the disc settles down with a small-scale fountain flow ($\lesssim$ kpc) operating from $t = 70$ to 150 Myr.
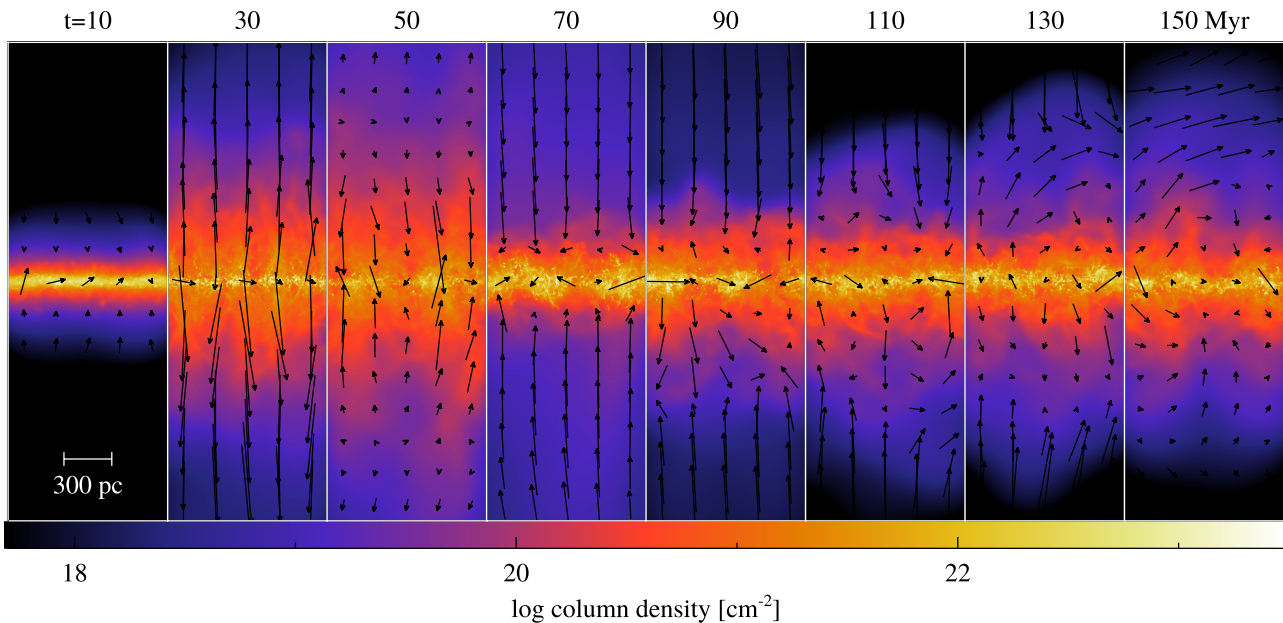
Figure 2. Same as Fig. 1 but for the PH simulation.

70 (fourth column), 90 (fifth column), 110 (sixth column), 130 (seventh column), and 150 (eighth column) Myr. The black arrows indicate the direction of the mass-weighted velocity field with the length of the arrows representing is magnitude. During the initial 10 Myr, the disc cools and contracts before the first stars form and explode as SN. This causes a small-scale inflow which reduces the scale height of the disc and induces a starburst. As the stars begin injecting feedback energy into the ISM, it starts to drive an outflow. This outflow period lasts up to $\sim$50 Myr, during which

time the disc scale height increases. The outflow reaches up to $\sim$4 kpc, stalls and begins to fall back to the disc. This inflow period lasts up to 75 Myr. The disc then settles down and forms stars at a constant rate which creates a small-scale ($\lesssim$1 kpc) fountain flow. The outflow velocities generated during the starburst phase of evolution are generally higher compared to the fountain flow phase.

The morphological evolution of the disc in the PH (Fig. 2), RP (Fig. 3), and IR (Fig. 4) simulations is qualitatively quite similar, with a prominent starburst-driven outflow phase followed by an
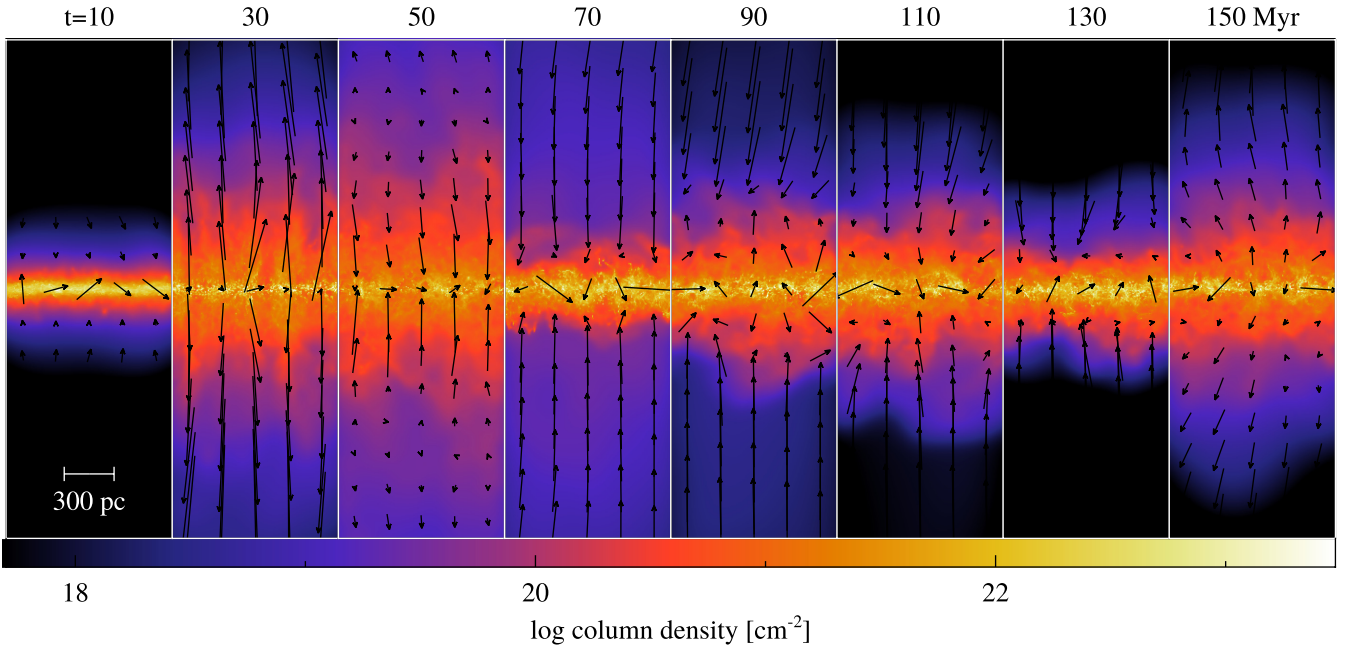
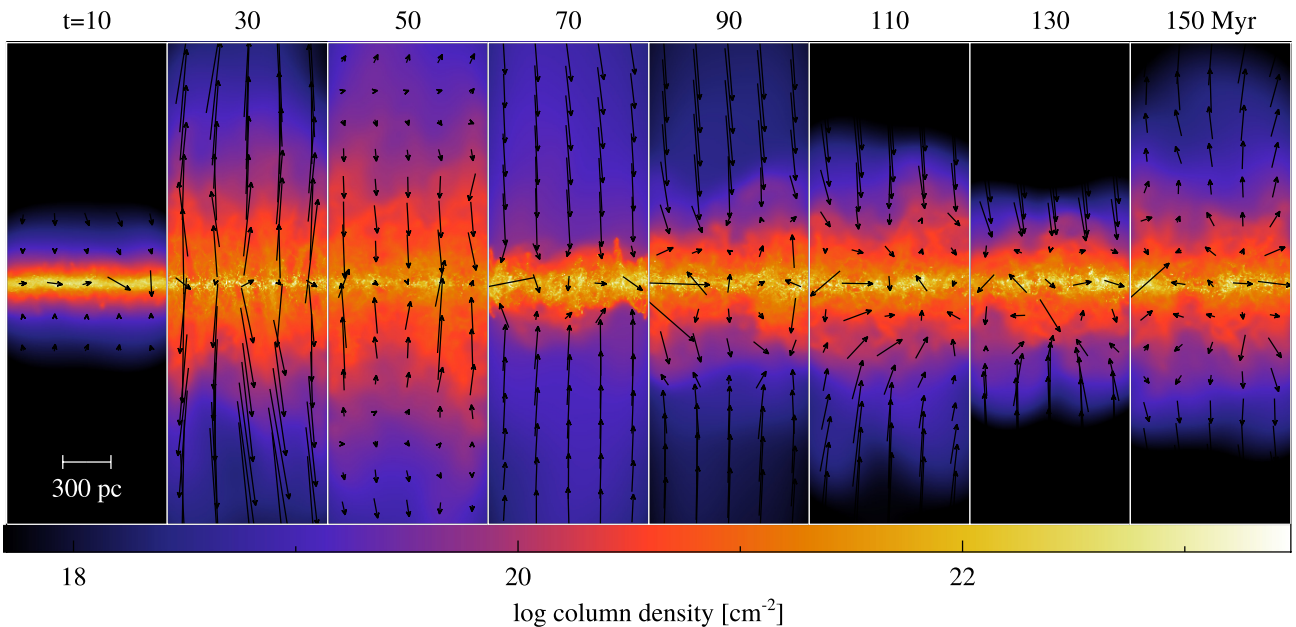**Figure 3.** Same as Fig. 1 but for the RP simulation.

Figure 4. Same as Fig. 1 but for the IR simulation.

inflow phase and a small-scale fountain flow phase. However, there are some interesting differences between the SN run and the runs with radiative feedback (or runs with early stellar feedback or ESF runs). Throughout the simulation, the central high-density disc remains relatively unperturbed in the SN run while the ESF runs manage to make the ISM more clustered creating low-density holes and filamentary channels through which material can be ejected without hindrance. This allows the ESF runs to drive gas flows to larger heights above the disc. This difference is clearly visible during the initial starburst period ($t = 30$–$50\,\mathrm{Myr}$). They are also able to entrain more high-density material in the outflow in both the starburst and fountain flow period of the evolution. These column density maps show that that including radiative feedback makes

stellar feedback qualitatively more effective. Most of the difference is seen between the SN and PH runs and there is very little difference between the PH, RP, and IR runs, implying that photoheating is the primary mechanism through which radiation interacts with the ISM and radiation pressure has minimal effect in regulating star formation and driving outflows in our model.

3.1 Star formation rate and the Kennicutt–Schmidt relation

We begin a more quantitative comparison by plotting the SFR surface density (top panel) and the total stellar mass formed (bottom panel) with time (Fig. 5) in the SN (red curves), PH (green curves), RP (blue curves), and IR (cyan curves) simu-
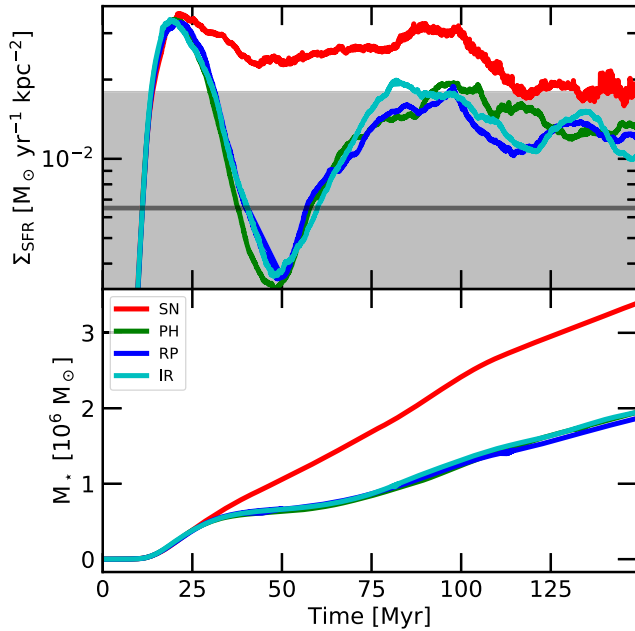
Figure 5. The SFR surface density (top panel) and the total amount of stellar mass formed (bottom panel) as a function of time (in Myr) in the SN (red curves), PH(green curves), RP (blue curves), and IR (cyan curves) simulations. The solid grey line depicts the expected SFR from the Kennicutt–Schmidt relation (Kennicutt & Evans 2012) and the grey shaded region is the factor of three observational error in the observed relation. After the initial starburst, the simulations with ESF show a steep drop in the SFR, which slowly bounces back and regulates to a value by a factor of approximately two times lower than in SN run. The total amount of stars formed is also reduced by a factor of ∼1.5 in the runs with ESF. The negligible difference between the PH, RP, and IR runs shows the inability of radiation pressure (both single and multiscattering) to regulate star formation in low surface density galaxies.

Figure 6. The SFR surface density as a function of the hydrogen (H + H₂) surface density in the SN (red), PH (green), RP (blue), and IR (cyan) simulations. The data are taken at the simulation time of $t = 150$ Myr. The individual points are obtained by dividing the disc into patches of size 100×100 pc and calculating both quantities for each patch. The solid lines denote the median for each simulation. For comparison, the observational estimates from Leroy et al. (2008) are plotted with black circles with the median relation plotted as the solid black line. The runs with ESF tend to bring the values close to the observed estimates.

lations (Please note that we will use this same colour scheme throughout this work.). The solid grey line depicts the expected SFR ($\Sigma_{SFR} = 6 \times 10^{-3} \, M_\odot \, yr^{-1} \, kpc^{-2}$ for $\Sigma_{gas} = 10 \, M_\odot \, pc^{-2}$) from the Kennicutt–Schmidt relation (Kennicutt 1998; Leroy et al. 2008; Kennicutt & Evans 2012) and the grey shaded region is the factor of three observational error in the observed relation. The amplitude of the initial starburst is similar in all simulations. This is expected because the stars have not had the time to feed energy back into the ISM. After about 20 Myr, the SFR curves start to deviate. The SN run continues to form stars at a very high rate ($\sim 0.02 - 0.03 \, M_\odot \, yr^{-1} \, kpc^{-2}$), while all three runs with radiative feedback show a precipitous drop in the SFRs, with the minimum as low as $\sim 0.003 \, M_\odot \, yr^{-1} \, kpc^{-2}$. By about 75 Myr the SFRs bounce back and saturate to a value that is about 1.5–2 lower than the SFRs obtained from the SN simulation. The SFR in the SN run always remains above the observed value throughout the simulation, matching the SFR estimates from the simulation including only SN feedback presented in Peters et al. (2017). We note that the drop off in the SFR surface density at about ∼100 Myr is due to a significant decrease in the gas surface density by ∼ 30 per cent due to the conversion of gas into stars. The ESF runs on the other hand manage to contain the SF within observational limits, even with higher gas surface density at late times, though it must be noted that it is at the upper end of the observed error margin. The total stellar mass formed in the ESF runs are also about a factor of two lower than the SN simulation. There is very little difference
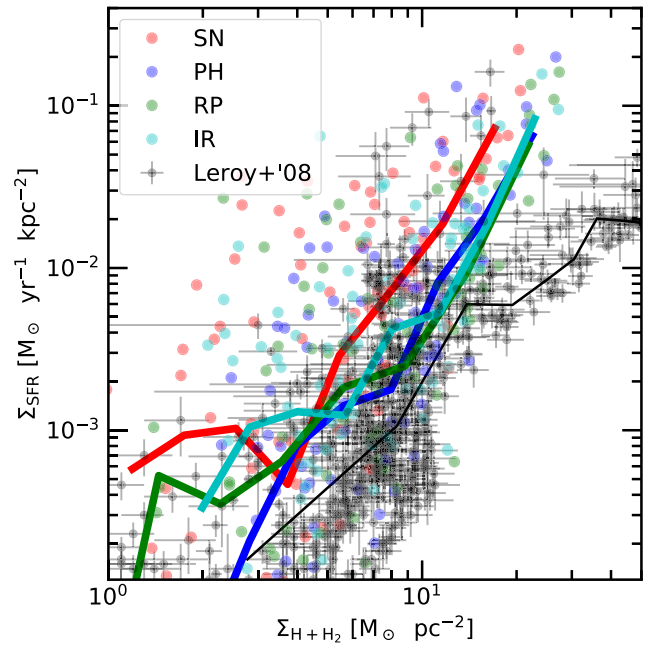
between the PH, RP, and IR runs, implying that radiation pressure, both UV and IR, is unimportant in these low-density environments. Photoheating therefore emerges as the most important early stellar feedback mechanism, which is in agreement with previous works (Sales et al. 2014; Rosdahl et al. 2015).

Fig. 6 shows the SFR surface density as a function of the gas (H + H₂) surface density at $t = 150$ Myr, for the simulations. The observational data points (black circles) are obtained from observations of 23 nearby galaxies as outlined in Leroy et al. (2008). The solid black curve shows the median of the observational points. The individual data points from our simulations are obtained from dividing the disc into 100×100 pc chunks and calculating both the quantities for each chunk. This allows us to study the KS relation in a wide variety of environments. The solid lines indicate the median values, which generally lie within the cloud of observed data points. Including radiative feedback brings the simulated KS relation closer to the observed values. We do, however, somewhat overshoot the relation, especially at high gas surface densities, possibly hinting at missing important physical processes like stellar winds (Gatto et al. 2017), cosmic rays (Simpson et al. 2016), or the effect of observed runaway massive stars ejected from their birth clouds and exploding in low-density environments (Girichidis et al. 2016b).

3.2 Outflow properties

We now turn our attention to the key quantities that describe an SN-driven wind, the mass (η_M), and energy (η_E) loading factors. The mass loading factor at a height z from the plane of the disc is
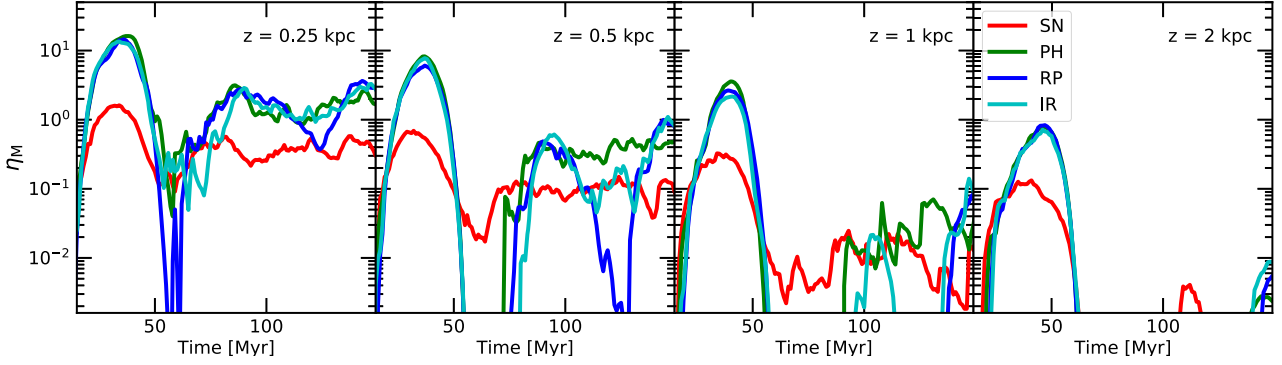
Figure 7. The mass loading factor (defined as $\eta_M = \dot{M}_{out}/\dot{M}_\star$) as a function of time at $z = 0.25$ (first panel), $z = 0.5$ (second panel), $z = 1.0$ (third panel), and $z = 2.0$ (fourth panel) kpc above the disc for the SN (red curves), PH (green curves), RP (blue curves), and IR (cyan curves) simulations. η_M generally decreases with z for all the runs and the runs with ESF generally have higher η_M's at all times.

defined as the ratio between the outgoing mass flux and the SFR:

$$\eta_M|_z = \frac{\dot{M}_{out}(z)}{\dot{M}_\star} . \tag{8}$$

Similarly, the energy loading factor at z is defined as the ratio of the total energy flux carried away by the wind to the energy injection rate by SN:

$$\eta_E|_z = \frac{\dot{E}_{kin,out} + \dot{E}_{therm,out}}{E_{SN}\dot{M}_\star} , \tag{9}$$

where $E_{SN} = 10^{51}$ erg/100 M$_\odot$. M_{out} and E$_{out}$ are calculated only for gas that has a z velocity vector pointing away from the disc mid-plane (i.e. we do not include any inflowing gas in our analysis of mass and energy loading factors). It is important to quantify these quantities as sub-grid feedback models generally prescribe the mass, energy, and metal loading factors and tune them in order to reproduce the observed galaxy properties (Vogelsberger et al. 2013).

Fig. 7 shows the mass loading factor at 0.25 kpc (first panel), 0.5 kpc (second panel), 1 kpc (third panel), and 2 kpc (fourth panel) above the disc for the simulations. The behaviour of η_M is qualitatively similar in all the runs, with its value peaking during the initial starburst-driven outflow phase, followed by a decrease during the inflow phase and a rebound, at least close to the disc, during the fountain flow period. During the initial starburst period, the SN simulation drives outflows with a mass loading of ~ 2 at $z = 0.25$ kpc which gradually drops to a value of about ~ 0.1 at $z = 2$ kpc. This weak outflow leaves the disc relatively unaltered, which allows the SF to continue at a relatively high rate even during the post-starburst period. The slight decrease in the SFR leads to a nominal decrease in η_M at low z ($\lesssim 1$ kpc). The mass loading at high z's, however, shows a large drop off because the lower SFRs combined with a puffier disc makes SN feedback less efficient. Under these conditions feedback is able to drive only a small-scale fountain flow up to a height of $z \sim 1$ kpc.

The quantitative picture in the ESF runs is quite different. The peak mass loading is much higher with a value of ~ 20 close to the disc and ~ 1 at $z = 2$ kpc. This blows out most of the gas from the disc causing the large drop off in the SF (see Fig. 5) during the post-starburst phase of the simulations. During this phase of evolution ($t = 25$–50 Myr), η_M in the ESF runs drops precipitously. This is caused by the large drop off in the star formation by almost a order of magnitude which reduces the pressure behind the outflow, making

it stall and fall back on to the disc. Once the disc settles down η_M rebounds to values of about two to three close to the disc, while there is very little outflowing gas at $z \gtrsim 1$ kpc. We note that this value is higher than that obtained in the SN simulation by a factor of five to 10. It is quite clear that a true large-scale wind is only launched during the initial starburst phase, while only a small-scale fountain flow operates after $t > 75$ Myr in all the runs. The initial starburst in our simulations is caused by the gas radiatively cooling, loosing its pressure support and settling down in the external gravitational potential into a thin disc. This is compounded by the fact that the main channel of feedback in our simulations, SN, are only active 5 Myr after the first stars form. Therefore, self-regulation during this initial period is not possible. Changes in initial conditions and parameters such as the time period between star formation and SN feedback will change the duration and strength of the starburst. While, the reasons for a starburst in the simulations are largely dictated by the way the initial conditions of our simulations are constructed, the difference between the evolution of SN and ESF simulations is quite dramatic and deserves further examination. Furthermore, an analogy can be made to the systems that have undergone a starburst during a merger making the scenario of a post-merger starburst-induced quenching in galaxies more probable.

Fig. 8 shows the energy loading factor at 0.25 kpc (first panel), 0.5 kpc (second panel), 1 kpc (third panel), and 2 kpc (fourth panel) above the disc. The evolution of η_E is qualitatively quite similar to the evolution in η_M, with the peak η_E occurring at about the same time as the occurrence of peak η_M at $t \sim 30$ Myr, followed by a precipitous drop in the post-starburst period for the ESF runs and the existence of a small-scale fountain flow with low energy loading after $t \gtrsim 75$ Myr. Peak η_E in the ESF runs ranges from ~ 0.02 at $z = 0.25$ kpc to 3×10^{-3} at $z = 2$ kpc. Interestingly, the peak energy loading in the SN simulation remains constant at about 3×10^{-3} across different heights from the disc. At late times value of η_E in the ESF runs is about two to three times larger than in SN run close to the disc ($z \lesssim 1$ kpc). It is difficult to make any claims about η_E above this height because of the absence of outflowing material. We note that there seems to be a bounce in the mass and energy loading factors after about 120 Myr mainly in the RP run at 0.5 kpc. This is because, while all models produce a fountain flow, the height of the outflow in the RP run is just below 0.5 kpc while the other runs have fountain flows that reach just above this height. These are very slight differences that we account to slightly differing SFR histories and not to the effect of radiation pressure.
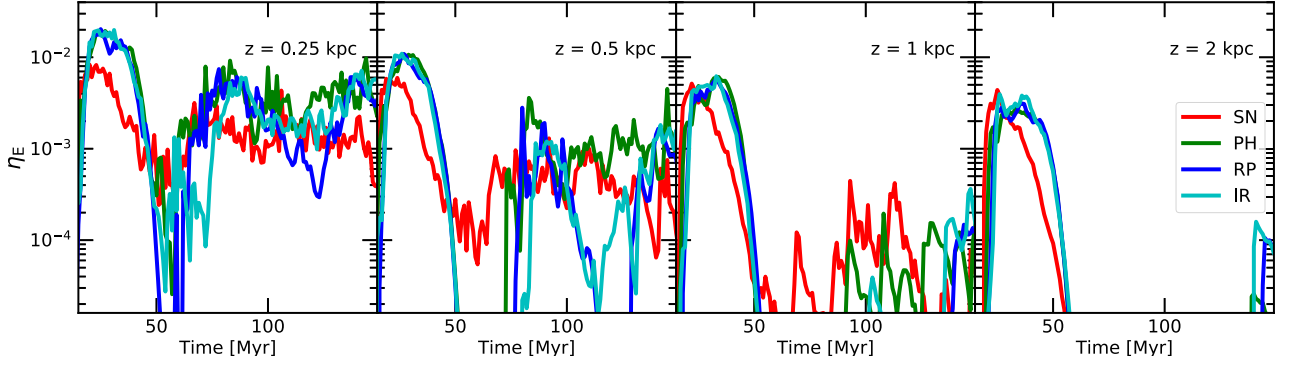
Figure 8. The energy loading factor (defined as $\eta_E = \dot{E}_{out}/\dot{E}_{SN}$) as a function of time at $z = 0.25$ (first panel), $z = 0.5$ (second panel), $z = 1.0$ (third panel), and $z = 2.0$ (fourth panel) kpc above the disc for the SN (red curves), PH (green curves), RP (blue curves), and IR (cyan curves) simulations.
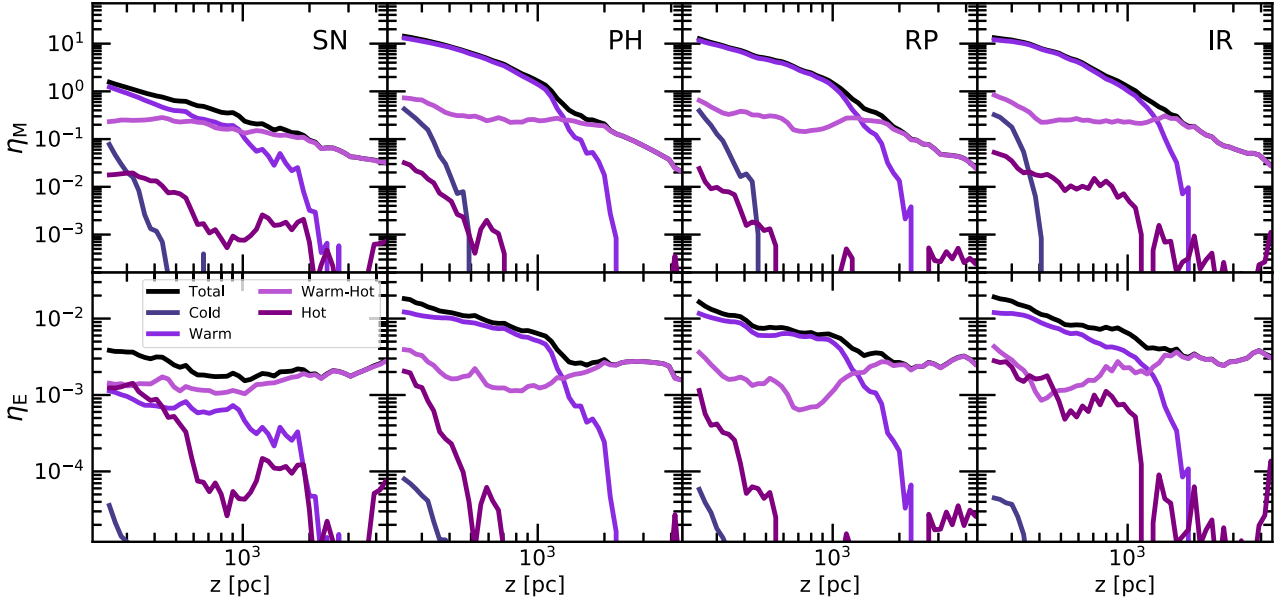

Figure 9. The mass (top panels) and energy loading (bottom panels) factors as a function of height from the disc (z) for cold ($T \leq 300$ K), warm (300 K $< T \leq 8000$ K), warm–hot (8000 K $< T \leq 3 \times 10^5$ K), and hot gas ($T > 3 \times 10^5$ K) during the outflow phase of the simulation, $t = 30$ Myr. The first column shows the values for the SN simulation, second column PH, third column RP, and the fourth column shows IR. Most of the mass and energy of the outflow is in the warm and warm–hot phases, with the cold and hot gas being subdominant. The increase in mass and energy loading factors in the runs with ESF is primarily driven by the increase in outflow of the warm phase.

3.2.1 Composition of the outflow during the starburst phase

A more comprehensive picture of the outflow behaviour can be obtained by decomposing (Fig. 9) the mass (top panels) and energy (bottom panels) loading into the different temperature bins at the peak of the outflow ($t = 30$ Myr) as a function of height from the disc. The dark blue curves indicate η_M and η_E for cold ($T < 300$ K) gas, violet curves for the warm (300 K $\leq T < 8000$ K) gas, orchid curves for the warm–hot (8000 K $\leq T < 3 \times 10^5$ K) gas, and purple curves for the hot ($T \geq 3 \times 10^5$ K) gas. Close to the disc, the SN run has a mass loading of about approximately two and decreases to 0.02 by $z \sim 4$kpc, and the energy loading remains constant at about 3×10^{-3}. The ESF runs on the other hand have η_M of $\sim$10 close to the disc, which reduces to $\sim$0.02 by about $\sim$4 kpc, while η_E ranges from 0.02 to $\sim 2 \times 10^{-3}$. Cold gas is never entrained in the outflow irrespective of the simulation we consider. The hot phase in the SN run has slightly more mass and energy loading compared to the ESF runs. However, both these phases are subdominant to

the warm and warm–hot gas phases. The warm–hot gas has roughly a constant mass ($\eta_M \sim 0.1$) and energy ($\eta_E \sim 2 \times 10^{-3}$) loading up to $z = 4$ kpc, implying the existence of a true large-scale wind (Kim & Ostriker 2018). Including radiative feedback only slightly increases η_M and η_E of this phase but drastically boosts it for the warm gas, especially at low z (<2 kpc). This effect is so large that the more mass and energy loading in the ESF runs at low z is almost entirely driven by the increase in the warm phase of the outflow. This implies that the runs with radiative feedback are able to entrain more warm material in the outflow and eject it to distances of about 2 kpc from the disc. Therefore, the ESF runs launch a more pronounced small-scale warm fountain flow in addition to the large-scale warm–hot wind during the starburst phase. This also explains the almost constant total energy loading in the SN run, contrasted to the declining energy loading in the ESF runs.

A similar analysis can be performed by decomposing the outflow into star forming ($n \geq 10^2$ cm^{-3}; dark blue curves), high (1 cm$^{-3} \leq n < 10^2$ cm^{-3}; violet curves), medium (10^{-2} cm$^{-3} \leq n < 1$ cm^{-3};
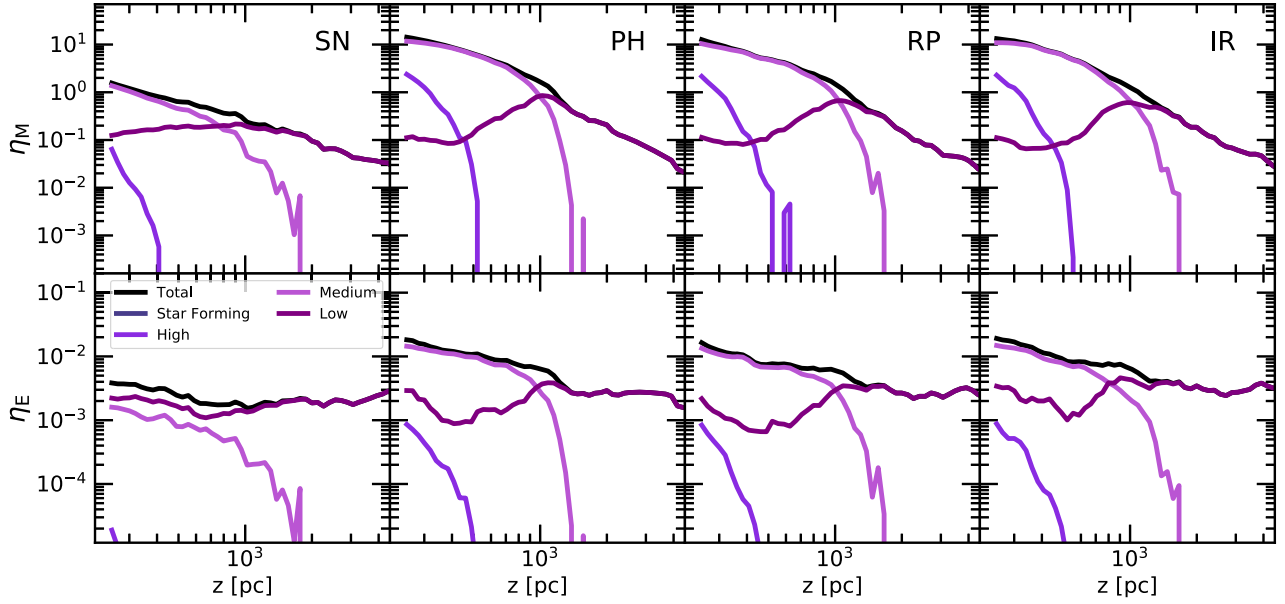
Figure 10. The mass (top panels) and energy loading (bottom panels) factors as a function of height from the disc (z) for star forming ($n \geq 10^2$ cm^{-3}), high (1 cm$^{-3} \leq n < 10^2$ cm^{-3}), medium (10^{-2} cm$^{-3} \leq n < 1$ cm^{-3}), and low ($n < 10^{-2}$ cm^{-3}) density gas during the outflow flow phase of the simulation, $t = 30$ Myr. The first column shows the values for the SN simulation, second column PH, third column RP, the fourth column shows IR.

orchid curves), and low ($n < 10^{-2}$ cm^{-3}; purple curves) density gas (Fig. 10). The density structure of the outflow in many ways mirrors its temperature structure. There is no entrainment of the star-forming gas in any of the runs. Some amount of high-density gas is launched up to heights of $z \lesssim 0.5$ kpc and the η_M and η_E for this phase in the ESF runs is about 10 times larger than in the SN run. The outflow is mostly dominated by the medium- and low-density material. The medium-density gas forms a fountain flow that reaches heights of $z \lesssim 2$ kpc while the low-density material forms a true large-scale wind. The mass and energy loading of the low-density wind is quite similar in the SN and ESF runs, but the medium-density fountain flow is about 10 times more mass and energy loaded in the ESF runs compared to the SN run. Therefore, a picture emerges of a starburst-driven outflow that can be decomposed into two distinct phases, a small-scale ($\sim$2 kpc) fountain flow mainly composed of warm (300 K $\leq T < 8000$ K), medium-density (0.01 cm$^{-3} \leq n < 1$ cm^{-3}) gas, and a large-scale wind ($\gtrsim 4$ kpc) that is composed of warm–hot (8000 K $\leq T < 3 \times 10^5$ K) low-density ($n < 10^{-2}$ cm^{-3}) material. We conclude that radiative feedback coupled with SN have the effect of launching colder, denser, and more mass-loaded outflows compared to the SN only case.

In order to better understand the mutiphase multicomponent nature of the outflow, we plot (Fig. 11) the temperature-outflow velocity (top panels) and density-outflow velocity (bottom panels) histograms in the SN (first column), PH (second column), RP (third column), and IR (fourth column) simulations. This plot considers all the gas that is moving outwards from the disc and at a height $z > 250$ pc as part of the outflow. The green horizontal lines divide the outflow into star-forming, high-, medium-, and low-density gas and similarly into cold, warm, warm–hot, and hot gas. There is a very clear trend towards higher velocities for higher temperature and lower density gas. The amount of gas mass in the outflow is much larger in the runs with radiative feedback. ESF runs are also able to entrain more cold and high-density material. The velocity of this phase is however less than $\sim$100 km s^{-1}, meaning that it cannot get very far from the disc, thereby generating a small-scale

fountain flow. The material with velocities larger than 100 km s^{-1} goes on to generate the large-scale wind which is both low density and hot. This explains the mass and energy loading behaviour of the outflows in our simulations. We note that the outflows generated in our simulations will not be able to reach wind velocities large enough to be unbound from the galaxy because the Milky Way escape velocity at the solar circle is $\sim$500 km s^{-1} (Smith et al. 2007).

3.2.2 Composition of the outflow during the fountain flow phase

A similar analysis can be performed in the fountain flow phase of the simulation ($t > 75$ Myr). Figs 12 and 13 decompose the mass (top panels) and energy (bottom panels) loading into the different temperature and density bins, respectively, during the fountain flow phase of the simulation at $t = 150$ Myr as a function of height from the disc. The mass and energy loading factors are lower than in the starburst phase as expected. Moreover, they decline quite steeply as the height above the disc increases, which is a clear sign of a fountain flow. Close to the disc, the SN run has a mass loading of about $\sim$0.2 and decreases to $<10^{-3}$ by $z \sim 1$ kpc, the energy loading goes from 6×10^{-4} to $\lesssim 10^{-4}$ in the same range. The ESF runs on the other hand have η_M of about $\sim$2 close to the disc which reduces to $\sim 10^{-3}$ at about $\sim$4 kpc and η_E ranges from 3×10^{-3} to $\sim 5 \times 10^{-4}$. In the SN run, none of the temperature or density phases reach beyond $z \gtrsim 1$ kpc. This is not the case in the runs with radiative feedback, where the warm–hot and low-density material reaches heights of $\sim$3 kpc. Above this height the hot low-density gas starts to dominate the (extremely weak) outflow.

Fig. 14 shows the the temperature-outflow velocity (top panels) and density-outflow velocity (bottom panels) histograms. The amount of mass in the outflow is much lower than during the starburst phase. The cold high-density phase no longer exists. There is very little gas with velocities $v_z \gtrsim 100$ km s^{-1}, explaining the lack of a large-scale wind. In the runs with radiative feedback, most of the gas is photoionized and has a temperature of $\sim 10^4$ K. The medium-density warm–hot phase is more mass loaded in the ESF runs
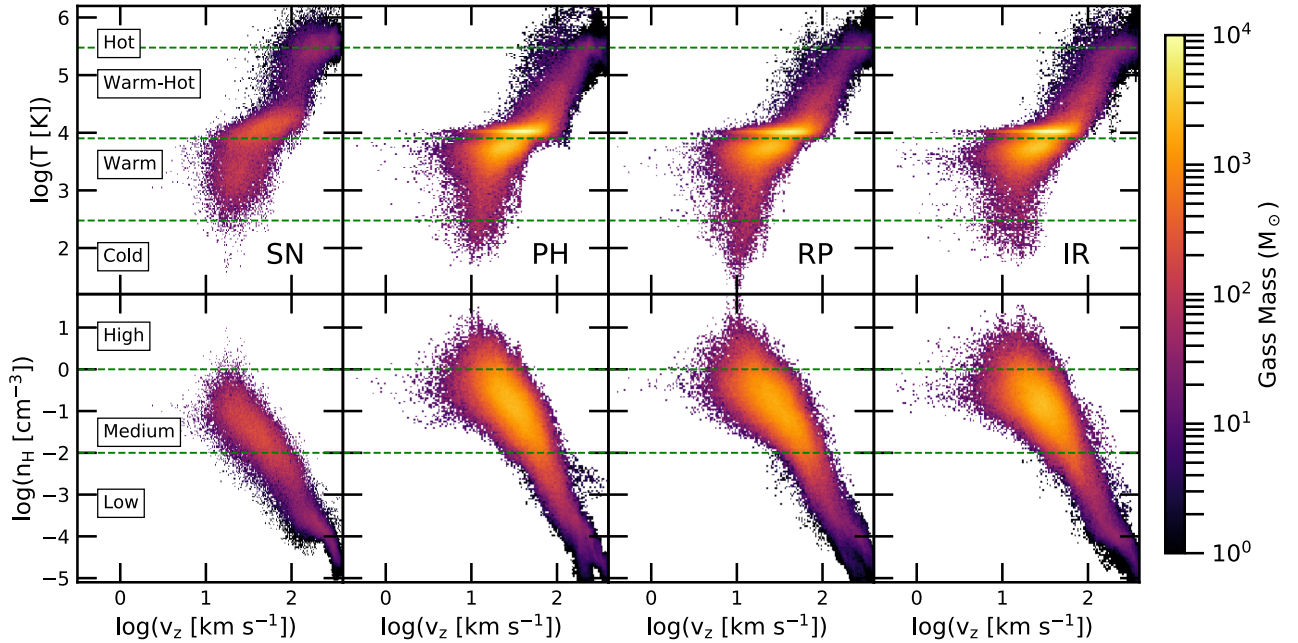
Figure 11. The temperature (top panels) and density (bottom panels) histograms of the outflowing gas as a function of the outflow velocity at $t = 30$ Myr for the SN (first column), PH (second column), RP (third column), and IR (fourth column) simulations.
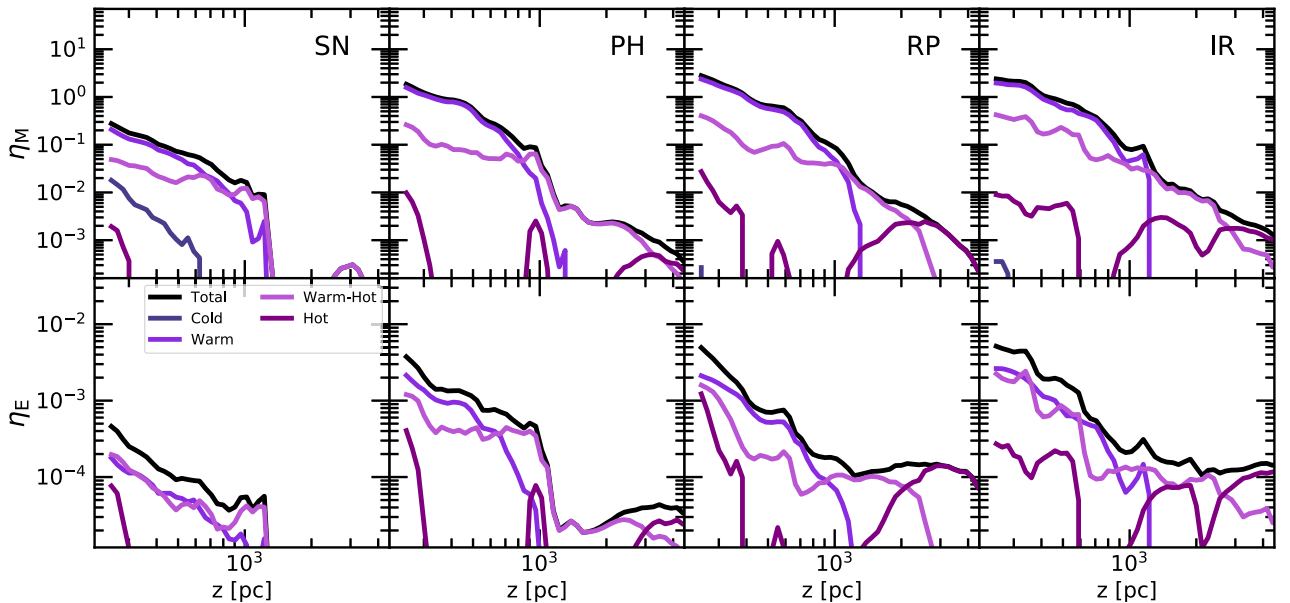

Figure 12. The mass (top panels) and energy loading (bottom panels) factors as a function of height from the disc (z) for cold ($T \le 300$ K), warm (300 K $< T \le 8000$ K), warm–hot (8000 K $< T \le 3 \times 10^5$ K), and hot gas ($T > 3 \times 10^5$ K) during the fountain flow phase of the simulation, $t = 150$ Myr. The fist column shows the values for the SN simulation, second column PH, third column RP, the fourth column shows IR. η_M and η_E are lower than during the outflow phase of the simulation, but the trends are quite similar.

compared to the SN run. It is therefore quite clear that even in the low star formation mode of evolution, radiative feedback make stellar feedback more efficient. They do not generate large-scale winds, but are able to launch low-temperature higher density outflows that are more mass and energy loaded. These outflows reach heights of about 1–2 kpc from the disc, forming a robust fountain flow. In contrast, just SN feedback creates a weak fountain flow that consists of mainly very low-density hot gas. This is despite the fact that the ESF runs have about two times lower SFR than the SN run.

Importantly, η_M and η_E are about a factor of $\sim$5–10 larger in the presence of radiative feedback and this increase is mainly driven by the entrainment of warm medium-density material in the outflowing gas. This quantitative result holds true in both the starburst and fountain flow phases of the simulation therefore implying that this is a very robust prediction. We however caution that these predictions need to be tested in a wide variety of environments in order to make sure that the results are independent of the simulation set-up and model parameters.
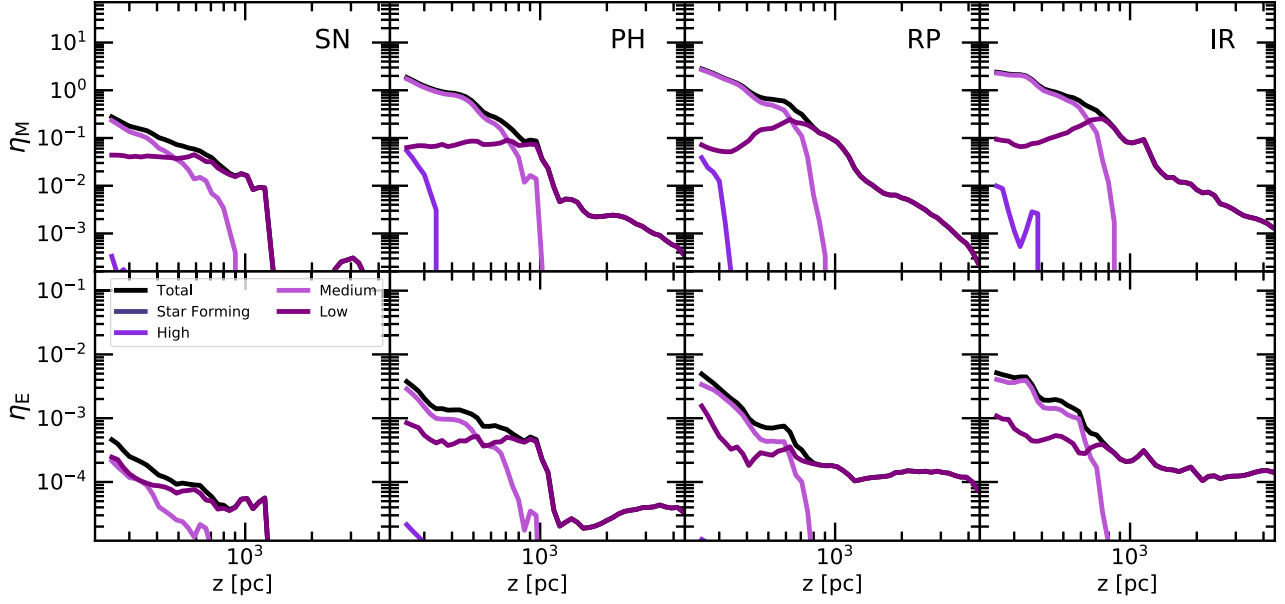
Figure 13. The mass (top panels) and energy loading (bottom panels) factors as a function of height from the disc (z) for star forming ($n \geq 10^2\,\mathrm{cm}^{-3}$), high ($1\,\mathrm{cm}^{-3} \leq n < 10^2\,\mathrm{cm}^{-3}$), medium ($10^{-2}\,\mathrm{cm}^{-3} \leq n < 1\,\mathrm{cm}^{-3}$), and low ($n < 10^{-2}\,\mathrm{cm}^{-3}$) density gas during the fountain flow phase of the simulation, $t = 150\,\mathrm{Myr}$. The fist column shows the values for the SN simulation, second column PH, third column RP, the fourth column shows IR.
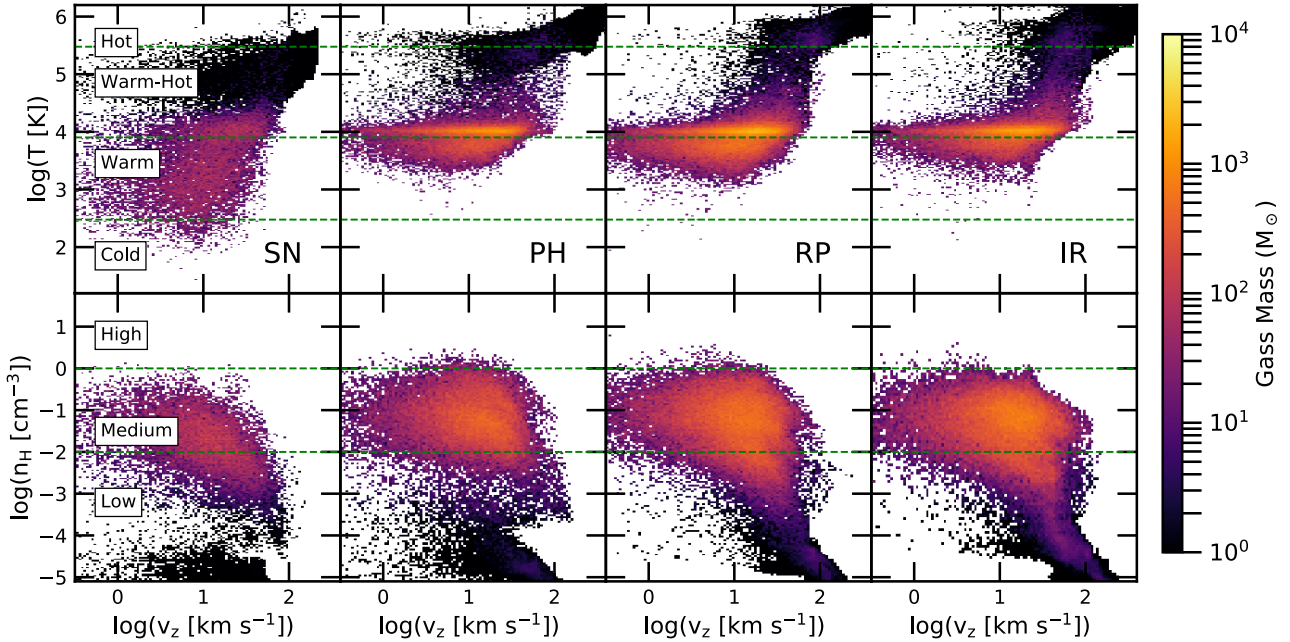

Figure 14. The temperature (top panels) and density (bottom panels) histograms of the outflowing gas as a function of the outflow velocity at $t = 150\,\mathrm{Myr}$ for the SN (first column), PH (second column), RP (third column), and IR (fourth column) simulations.

3.2.3 Chemical composition of the outflow

To assess the impact of stellar radiation on the chemical composition of the outflowing gas, we plot in Fig. 15 the masses of the ejected material in terms of different hydrogen species as a function of time. The ejected material is defined as any gas present above $z = 250\,\mathrm{pc}$ at any given point in time. The first column shows the total amount of ejected gas, the second column mass in molecular hydrogen H_2, third column neutral hydrogen, and the fourth column shows mass of ionized hydrogen. As expected, the total amount of gas ejected from the disc is higher in the ESF runs, by about a factor of approximately

five during the starburst period and approximately two at the later stages ($t \gtrsim 75\,\mathrm{Myr}$). The fraction of gas in the molecular state is quite low (< 5 per cent) in all the runs. This is expected because the density of gas at these heights is quite low ($<1\,\mathrm{cm}^{-3}$). However, the lack of any radiation in the SN run allows for a comparatively large molecular fraction in the outflow. This picture will definitely change if the metagalactic background is included. Finally, we note that the illumination of the ejected gas by the radiation from the disc increases the abundance of ionized hydrogen by a factor of ~ 10. Therefore, we conclude that the ESF runs give rise to ejecta that is
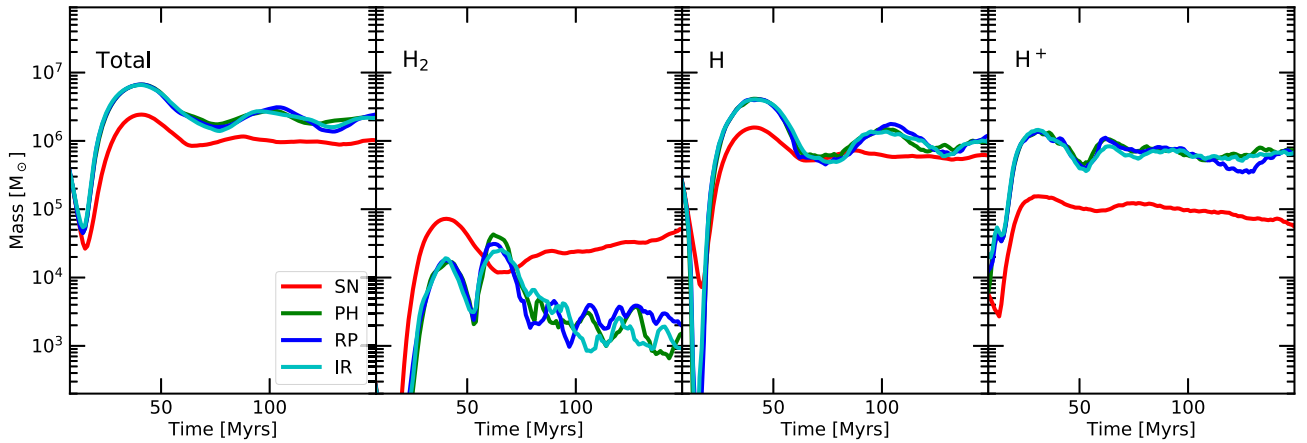
Figure 15. The chemical composition of the ejected outflow as a function of time in the SN (red curves), PH (green curves), RP (blue curves), and IR (cyan curves) simulations. The ejected material is defined as any material with $z > 250$ pc. The first column shows the total amount of ejected gas, the second column mass in molecular hydrogen (H_2), third column neutral hydrogen, and the fourth column shows mass of ionized hydrogen.

half ionized and half neutral, whereas the ejecta in the SN run is mainly neutral due to the absence of stellar radiation.

4 DISCUSSION

On the whole, the runs with radiative feedback increase the mass and energy loading factor by about a factor of 5–10, close to the disc ($z < 1$ kpc), for most of the duration of the simulation. They are still lower by about two to three when compared to random driving (SN explosions occur at random positions) tallbox simulations presented in Girichidis et al. (2016a). The motivation of our simulations was to get the structure of the ISM right, meaning that the mass and energy loading factors were not tuned to match observations. On the other hand, our values are closer to those predicted by global galaxy simulations with more realistic geometries (Muratov et al. 2015; Fielding et al. 2017) and with analytic estimates of the values required to explain the observed galaxy stellar mass function and the metal enrichment of the intergalactic medium (Somerville & Davé 2015). However, our tallbox geometry implies that the wind mass and energy loading factors are not well defined because they decrease quite substantially with increasing box height (See Section 5 for more details). Despite this caveat, it is quite clear that early stellar feedback does indeed play an important role in regulating star formation and launching outflows. The consistently lower SFRs in the ESF runs indicate that radiative feedback makes stellar feedback more efficient. There are two ways in which the radiative feedback can reduce star formation. They can heat up the disc through photoheating, which increases the temperature in the disc, puffing it up and reducing the star formation. Secondly, photoheating can evacuate gas from the neighbourhood of newly formed stars allowing them to explode in relatively low-density environments. This increases the momentum output of SN explosions by reducing the cooling losses (Martizzi et al. 2015). There is evidence for both these effects in our simulations.

Fig. 16 shows the temperature–density (top panels) and pressure–density (bottom panels) phase-space diagram of the gas in the disc (defined as $z < 250$ pc) at $t = 150$ Myr in the SN (first column), PH (second column), RP (third column), and IR (fourth column) simulations. The black solid lines show the median of the distribution. For comparison, the median obtained from the SN simulation is plotted in the ESF runs in solid green lines. Only the ESF runs show a true two-temperature multiphase medium

in pressure equilibrium. For a given density the temperature and therefore the pressure of the gas is higher in the runs with radiative feedback.[1] This higher pressure provides additional support against gravitational collapse, puffing up the disc and reducing the SFR. This effect can be quantified by looking at the vertical structure of the disc. A simple estimate is obtained by calculating the height which encloses 60 per cent of the total mass of the disc ($H_{60\,per\,cent}$) and contrasting it with $H_{90\,per\,cent}$, the height which encloses 90 per cent of the total mass. $H_{60\,per\,cent}$ gives us an estimate of the distribution of the dense molecular gas in the disc, while $H_{90\,per\,cent}$ informs us about the envelope of the disc. Fig. 17 shows the time evolution of $H_{60\,per\,cent}$ (top panel) and $H_{90\,per\,cent}$ (bottom panel) for all the simulations. For the initial ~ 10 Myr, the disc cools and contracts reducing $H_{60\,per\,cent}$ to ~ 10 pc and $H_{90\,per\,cent}$ to ~ 20 pc. This gas compression leads to a starburst-induced outflow leading to an increase in both $H_{60\,per\,cent}$ and $H_{90\,per\,cent}$. The stronger outflows in the ESF runs cause $H_{90\,per\,cent}$ to reach a peak of about ~ 600 pc at $t = 40$ Myr, while it only increases to about ~ 200 pc in the SN run. At the same time $H_{60\,per\,cent}$ increases to ~ 200 pc in the ESF runs and ~ 60 pc in the SN run. Both heights decrease during the inflow period and then rebound back and remain fairly constant after $t > 75$ Myr. At these late times, the difference in $H_{90\,per\,cent}$ between the SN (~ 150 pc) and ESF runs is quite nominal (~ 200 pc), with the ESF runs having a larger value by about 50 per cent. $H_{60\,per\,cent}$, on the other hand, shows about a factor of two increase in the ESF (~ 60 pc) runs. This implies that the discs in ESF runs are more puffed up due to additional pressure from the photoheated gas, which in turn reduces the density reducing the SFR.

It is also worth noting that the temperature and pressure difference between the SN and ESF runs in the high-density star-forming gas ($n_H \gtrsim 100 \, cm^{-3}$) is quite small, implying very little difference between the sites of star formation in the different runs. However, once the stars form, photoheating of high-density material around a newly formed star overpressurizes the region, which then expands till it reaches a pressure equilibrium with the surrounding gas. This reduces the density of the gas and causes a pile-up of material at

---

[1]We note that the diagonal/horizontal features in the temperature- and pressure-density plots, respectively, are constant pressure lines that arise naturally when the SN energy is injected in a volume-weighted fashion around a exploding star.
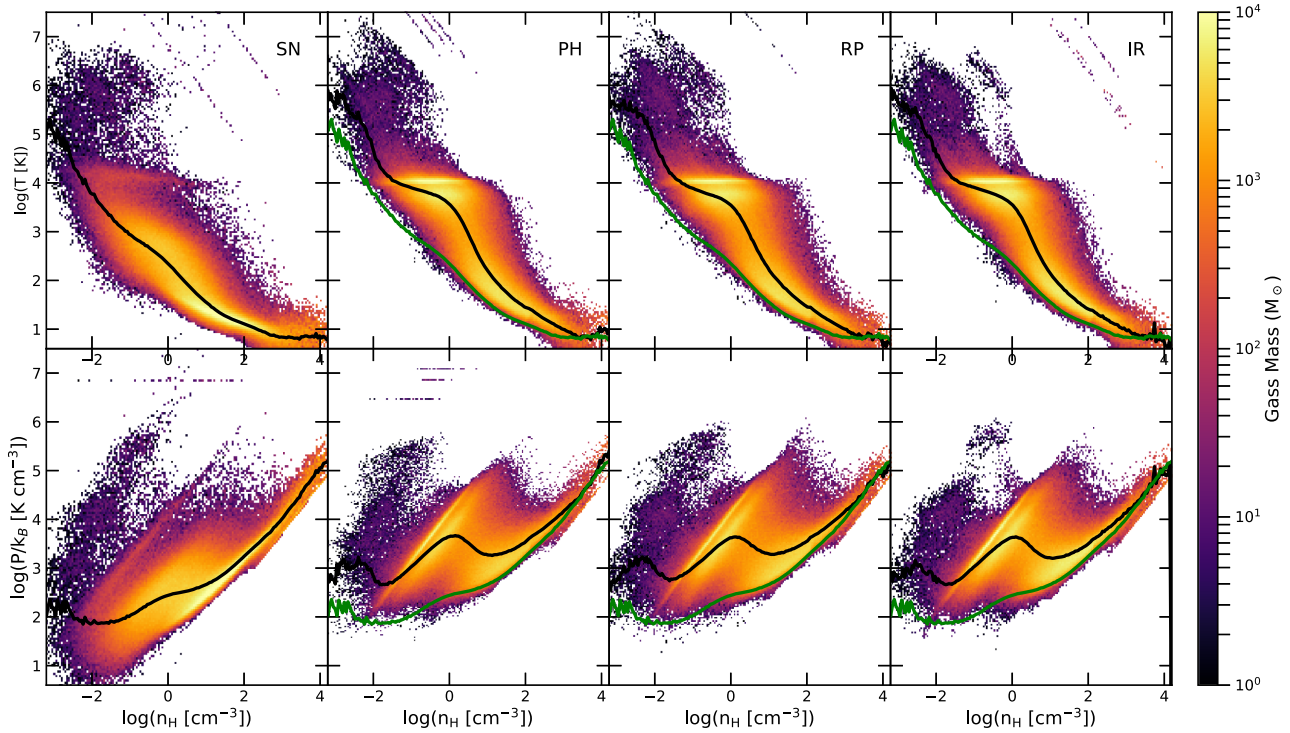
Figure 16. The temperature-density (top panels) and pressure-density (bottom panels) phase space diagram of the disc ($z < 250$ pc) at $t = 150$ Myr for the SN (first column), PH (second column), RP (third column), and IR (fourth column) simulations. In general, for a given density the gas temperature and therefore pressure is higher for the runs with ESF. The black lines denote the median of the distribution and the solid green lines in the ESF runs denote the median obtained from the SN simulation.

the photoheating temperature (about $\sim 10^4$ K for a soft spectra from stars), a prominent feature in the ESF runs. Direct evidence for this effect can be gained by looking at the mean densities at which the SN explode in the different runs. Fig. 18 plots the cumulative distribution of the number of SN as a function of the mean density at which they explode for all the simulations. In the SN run, about 50 per cent of the SN explode in star-forming high-density gas and about 90 per cent in gas with $n > 10\,\mathrm{cm}^{-3}$. Since the star formation density threshold is $n = 100\,\mathrm{cm}^{-3}$, this means that the stars in the SN run explode in the same high-density regions in which they form. On the other hand, in the ESF runs, more than 80 per cent of the SN explode in gas with $n < 10\,\mathrm{cm}^{-3}$ and more than 90 per cent in gas with $n < 100\,\mathrm{cm}^{-3}$, implying that radiative feedback combined with SN reduces the mean ambient density by a factor of about 10–100.

The evolution of an SN remnant in different density environments have been studied in great detail by many recent works (Kim & Ostriker 2015; Martizzi et al. 2015; Haid et al. 2016). Briefly, the evolution of the SN can be divided into four phases (McKee & Ostriker 1977): the pre Sedov-Taylor (PST) phase, the ST phase, the pressure-driven snowplough (PDS) phase, and finally the momentum conserving (MC) phase. During the PST phase, the SN ejecta runs into the ambient ISM shocking and thermalizing a large fraction of the injected energy. This then initiates an energy conserving ST phase, which ends when the rate of change of temperature due to adiabatic expansion is comparable to radiative losses. Finally, the PDS phase is defined by the domination of radiative cooling with the pressure inside the bubble driving the expansion of the SN remnant. During all these evolutionary phases the increased thermal pressure within the bubble pushes on the surrounding low-pressure ISM boosting the final momentum output of the SN event. Eventually, when the pressure inside the bubble becomes equal to the ambient

pressure, the remnant becomes momentum conserving. Simulations have shown that the momentum boost achieved in realistic ISM environments is about a factor of 9–25 depending on the ambient density in which the SN explodes. The duration of the ST and PDS phases depends on the cooling time of the gas, which in turn depends on the ambient density, with more cooling occurring in higher density gas ($t_{\mathrm{cool}} \propto n^{-0.55}$). The longer cooling times in low-density medium leads to a longer duration of the momentum boosting phases leading to more ISM material being swept up and accelerated to larger velocities, with the mass of the swept-up material scaling with ambient density as $M_{\mathrm{swept}} \propto n^{-0.26}$ which implies that a reduction in the ambient density by a factor of ~ 100 increases the mass of the swept material by about a factor of approximately three. Therefore, we can conclude that because SN explode in lower density environments in the ESF simulations, the duration of the momentum boosting phases is longer, leading to a higher amount of the colder denser ISM (compared to the hot wind) being swept up and accelerated to larger velocities in the outflow. This not only explains the increased mass and energy loading factors in the ESF runs, but also the increased entrainment of colder and denser gas.

Finally, we note that the resolved SN momentum budget has only a weak dependence on the density of the ambient medium $\Delta p \sim n^{-0.19}$ (Blondin et al. 1998; Thornton et al. 1998; Kim & Ostriker 2015; Martizzi et al. 2015; Haid et al. 2016). Using this scaling we can conclude that radiative feedback can increase the momentum output of the SN by a factor of about 1.5–2.5. This increased coupling efficiency combined with the fact that the radiative feedback provides additional pressure support against gravity explains the differences between the SN and ESF runs presented in this paper. These effects are in agreement with previous self-consistent RHD simulations presented in Rosdahl et al. (2015) and Peters et al. (2017).
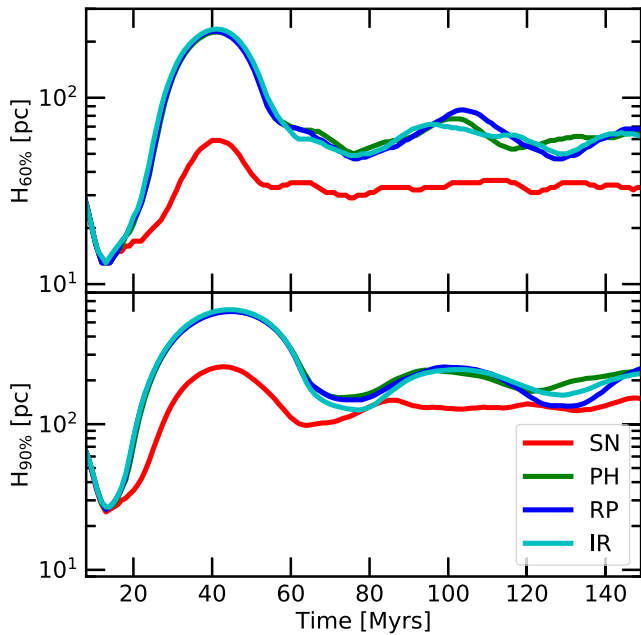
Figure 17. Vertical heights of 60 per cent (top panel) and 90 per cent enclosed mass as a function of time for the SN (red curves), PH (green curves), RP (blue curves), and IR (cyan curves) simulations. ESF increases the scale height of the disc almost a factor of approximately two.
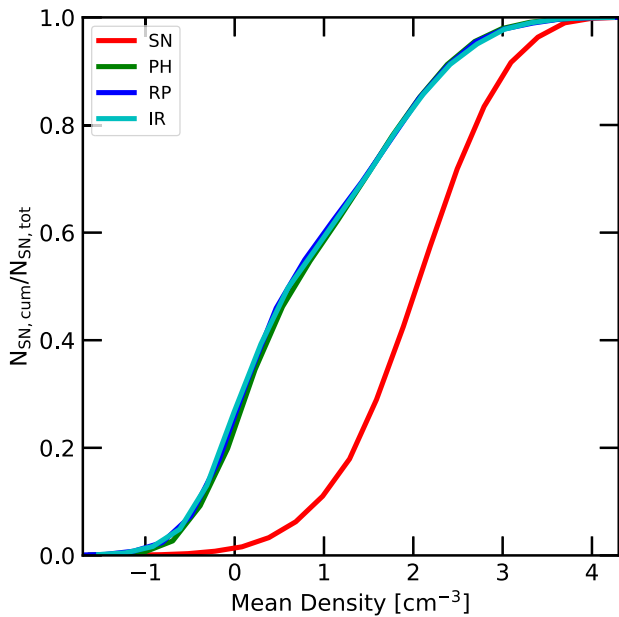

Figure 18. Normalized cumulative counts of the SNe as a function of the mean environmental density in which they explode for the SN (red curves), PH (green curves), RP (blue curves), and IR (cyan curves) simulations. Photoheating reduces the density at which the SN go off by a factor of 10–100, thereby increasing the momentum input of an SN feedback event.

5 CONCLUSIONS

In this paper, we present extremely high-resolution RHD simulations of a small patch of the ISM performed with AREPO-RT. We performed four simulations: SN: simulation with just SN feedback, PH: SN + photoheating from local stellar radiation, RP: PH + effect of UV radiation pressure, and IR: RP + effect of multiscattering IR

radiation pressure. These simulations were performed with a mass resolution of $10 \, M_{\odot}$ and a spatial resolution of $\sim$45 pc. This allows us to resolve all the included feedback processes, thereby providing us with an accurate picture of stellar feedback in low gas surface density galaxies. Our main results can be summarized as follows:

(i) Radiation fields have the effect of reducing the SFRs and thereby the total stellar mass of the galaxies by about a factor of approximately two. This has the effect of increasing the gas depletion time-scales in the simulations, thereby allowing for a better match with the observed Kennicutt–Schmidt relation.

(ii) The most important effect of radiative feedback is photoheating by ionizing photons. Radiation pressure, both single and multiscattered, does not have a significant effect in low gas surface density environments.

(iii) The mass and energy loading factors increase by $\sim$5–10 in the presence of radiative feedback. The increase is mainly driven by the additional entertainment of medium-density ($10^{-2} \, \mathrm{cm}^{-3} \leq n < 1 \, \mathrm{cm}^{-3}$) warm ($300 \, \mathrm{K} \leq T < 8000 \, \mathrm{K}$) material in the outflow. This material has velocities of about $\sim$10–100 km s^{-1}, meaning that it falls back on the disc creating a fountain flow of order $\sim$2 kpc. Radiation fields therefore help drive colder, denser, and more mass- and energy-loaded outflows compared to models that invoke only SN feedback.

(iv) The radiation from stars generates an interstellar radiation field (ISRF) that permeates through the disc increasing the temperature of the gas which in turn increases the pressure support of the gas against gravitational collapse. This puffs up the disc and reduces star formation.

(v) Photoheating of high-density material around a newly formed star overpressurizes the region, which then expands into the ISM. This reduces the ambient density in which the SN explode by a factor of 10–100, increasing their momentum input by a factor of $\sim$1.5–2.5.

The effect of radiation pressure is minimal when it acts together with photoheating because the amount of time needed to generate and launch significant small-scale winds is much shorter for photoheating (Sales et al. 2014; Geen et al. 2015). In the future, we plan to build upon this work and test the effect of radiation pressure in high surface density, star-bursting galaxies (Kleinmann et al. 1988) as well as in more massive giant molecular clouds in low surface density galaxies, as this mechanism is theorized to be more effective in these environments (Hopkins et al. 2011; Thompson et al. 2015; Rahner et al. 2017).

The relatively high SFRs even with radiative feedback hint that there might be additional feedback mechanisms that have not been accounted for in this work such as stellar winds (Gatto et al. 2017; Peters et al. 2017), cosmic rays (Simpson et al. 2016; Ruszkowski, Yang & Zweibel 2017; Diesing & Caprioli 2018), or magnetic fields (Kim & Ostriker 2015). We plan to include the effect of all three processes in a future work. Another caveat of this work is that the geometry of the tallbox set-up is not realistic. Previous works have shown that the properties of galactic winds are not accurately predicted because they do not capture the correct global geometry and gravitational potential of galaxies (Martizzi et al. 2016). The wind structure and outflow rates are not converged with respect to the box height. This is because in Cartesian geometry there are no adiabatic steady-state winds that undergo a subsonic to supersonic transition. The main impact is stalling of material at higher heights falling back down. However, this local tallbox set-up was required to achieve the resolution necessary to resolve relevant feedback processes in our simulations. We plan to run

physically realistic calculations (e.g. isolated full disc simulation) to fully understand the role of radiative feedback in launching galactic outflows in the future. While, we have only focused on the dynamical impact of early stellar feedback, radiation also changes the chemical composition of the ISM, which we will investigate in a future paper. We conclude by noting that early stellar feedback in the form of photoheating is an important physical process that enhances the effectiveness of SN feedback, a result that is in agreement with previous self-consistant RHD simulations (Rosdahl & Teyssier 2015; Gatto et al. 2017; Peters et al. 2017; Emerick et al. 2018), thereby confirming the important role that radiative feedback play in regulating star formation and determining the structure of the ISM and outflows in galaxies.

ACKNOWLEDGEMENTS

REFERENCES

Agertz O., Kravtsov A. V., Leitner S. N., Gnedin N. Y., 2013, ApJ, 770, 25
Baczynski C., Glover S. C. O., Klessen R. S., 2015, MNRAS, 454, 380
Blondin J. M., Wright E. B., Borkowski K. J., Reynolds S. P., 1998, ApJ, 500, 342
Bruzual G., Charlot S., 2003, MNRAS, 344, 1000
Cantalupo S., 2010, MNRAS, 403, L16
Chabrier G., 2003, PASP, 115, 763
Creasey P., Theuns T., Bower R. G., 2013, MNRAS, 429, 1922
Dalla Vecchia C., Schaye J., 2008, MNRAS, 387, 1431
Davé R., Thompson R., Hopkins P. F., 2016, MNRAS, 462, 3265
Davé R., Anglés-Alcázar D., Narayanan D., Li Q., Rafieferantsoa M. H., Appleby S., 2019, MNRAS, 486, 2827
Davis S. W., Jiang Y.-F., Stone J. M., Murray N., 2014, ApJ, 796, 107
Diesing R., Caprioli D., 2018, Phys. Rev. Lett., 121, 091101
Draine B. T., Bertoldi F., 1996, ApJ, 468, 269
Dubois Y., Peirani S., Pichon C., Devriendt J., Gavazzi R., Welker C., Volonteri M., 2016, MNRAS, 463, 3948
Emerick A., Bryan G. L., Mac Low M.-M., 2018, ApJ, 865, L22
Fielding D., Quataert E., Martizzi D., Faucher-Giguère C.-A., 2017, MNRAS, 470, L39
Gatto A. et al., 2017, MNRAS, 466, 1903
Geen S., Rosdahl J., Blaizot J., Devriendt J., Slyz A., 2015, MNRAS, 448, 3248
Girichidis P. et al., 2016a, MNRAS, 456, 3432
Girichidis P. et al., 2016b, MNRAS, 456, 3432
Glover S. C. O., Clark P. C., 2012, MNRAS, 421, 116
Glover S. C. O., Mac Low M.-M., 2007a, ApJS, 169, 239
Glover S. C. O., Mac Low M.-M., 2007b, ApJ, 659, 1317
Gnedin N. Y., Draine B. T., 2014, ApJ, 795, 37
Gnedin N. Y., Hollon N., 2012, ApJS, 202, 13
Guedes J., Callegari S., Madau P., Mayer L., 2011, ApJ, 742, 76
Haid S., Walch S., Naab T., Seifried D., Mackey J., Gatto A., 2016, MNRAS, 460, 2962

Hopkins P. F., Grudic M. Y., 2019, MNRAS, 483, 4187
Hopkins P. F., Quataert E., Murray N., 2011, MNRAS, 417, 950
Hopkins P. F., Kereš D., Oñorbe J., Faucher-Giguère C.-A., Quataert E., Murray N., Bullock J. S., 2014, MNRAS, 445, 581
Hopkins P. F. et al., 2018, MNRAS, 480, 800
Kannan R. et al., 2014a, MNRAS, 437, 2882
Kannan R., Stinson G. S., Macciò A. V., Brook C., Weinmann S. M., Wadsley J., Couchman H. M. P., 2014b, MNRAS, 437, 3529
Kannan R., Vogelsberger M., Stinson G. S., Hennawi J. F., Marinacci F., Springel V., Macciò A. V., 2016, MNRAS, 458, 2516
Kannan R., Vogelsberger M., Marinacci F., McKinnon R., Pakmor R., Springel V., 2019, MNRAS, 485, 117,
Katz N., Weinberg D. H., Hernquist L., 1996, ApJS, 105, 19
Kennicutt R. C., Jr, 1998, ApJ, 498, 541
Kennicutt R. C., Evans N. J., 2012, ARA&A, 50, 531
Kim C.-G., Ostriker E. C., 2015, ApJ, 815, 67
Kim C.-G., Ostriker E. C., 2017, ApJ, 846, 133
Kim C.-G., Ostriker E. C., 2018, ApJ, 853, 173
Kleinmann S. G., Hamilton D., Keel W. C., Wynn-Williams C. G., Eales S. A., Becklin E. E., Kuntz K. D., 1988, ApJ, 328, 161
Krumholz M. R., Thompson T. A., 2013, MNRAS, 434, 2329
Leitherer C. et al., 1999, ApJS, 123, 3
Leroy A. K., Walter F., Brinks E., Bigiel F., de Blok W. J. G., Madore B., Thornley M. D., 2008, AJ, 136, 2782
Machacek M. E., Bryan G. L., Abel T., 2001, ApJ, 548, 509
Marinacci F. et al., 2018, MNRAS, 480, 5113
Martizzi D., Faucher-Giguère C.-A., Quataert E., 2015, MNRAS, 450, 504
Martizzi D., Fielding D., Faucher-Giguère C.-A., Quataert E., 2016, MNRAS, 459, 2311
McKee C. F., Ostriker J. P., 1977, ApJ, 218, 148
Muratov A. L., Kereš D., Faucher-Giguère C.-A., Hopkins P. F., Quataert E., Murray N., 2015, MNRAS, 454, 2691
Murray N., Quataert E., Thompson T. A., 2010, ApJ, 709, 191
Naiman J. P. et al., 2018, MNRAS, 477, 1206
Navarro J. F., Frenk C. S., White S. D. M., 1996, ApJ, 462, 563
Nelson D. et al., 2018, MNRAS, 475, 624
Nelson R. P., Langer W. D., 1997, ApJ, 482, 796
Nickerson S., Teyssier R., Rosdahl J., 2018, MNRAS, 479, 3206
Oppenheimer B. D., Davé R., 2006, MNRAS, 373, 1265
Pakmor R., Springel V., Bauer A., Mocz P., Munoz D. J., Ohlmann S. T., Schaal K., Zhu C., 2016, MNRAS, 455, 1134
Peters T. et al., 2017, MNRAS, 466, 3293
Pillepich A. et al., 2018, MNRAS, 475, 648
Rahner D., Pellegrini E. W., Glover S. C. O., Klessen R. S., 2017, MNRAS, 470, 4453
Rosdahl J., Teyssier R., 2015, MNRAS, 449, 4380
Rosdahl J., Schaye J., Teyssier R., Agertz O., 2015, MNRAS, 451, 34
Roškar R., Teyssier R., Agertz O., Wetzstein M., Moore B., 2014, MNRAS, 444, 2837
Ruszkowski M., Yang H.-Y. K., Zweibel E., 2017, ApJ, 834, 208
Sales L. V., Marinacci F., Springel V., Petkova M., 2014, MNRAS, 439, 2990
Schaye J. et al., 2015, MNRAS, 446, 521
Simpson C. M., Bryan G. L., Hummels C., Ostriker J. P., 2015, ApJ, 809, 69
Simpson C. M., Pakmor R., Marinacci F., Pfrommer C., Springel V., Glover S. C. O., Clark P. C., Smith R. J., 2016, ApJ, 827, L29
Smith M. C. et al., 2007, MNRAS, 379, 755
Smith R. J., Glover S. C. O., Clark P. C., Klessen R. S., Springel V., 2014, MNRAS, 441, 1628
Somerville R. S., Davé R., 2015, ARA&A, 53, 51
Springel V., 2010, MNRAS, 401, 791
Springel V., Hernquist L., 2003, MNRAS, 339, 289
Springel V. et al., 2018, MNRAS, 475, 676
Sternberg A., Le Petit F., Roueff E., Le Bourlot J., 2014, ApJ, 790, 10
Stinson G., Seth A., Katz N., Wadsley J., Governato F., Quinn T., 2006, MNRAS, 373, 1074

Stinson G. S., Brook C., Macciò A. V., Wadsley J., Quinn T. R., Couchman H. M. P., 2013, MNRAS, 428, 129

Thacker R. J., Couchman H. M. P., 2001, ApJ, 555, L17

Thompson T. A., Fabian A. C., Quataert E., Murray N., 2015, MNRAS, 449, 147

Thornton K., Gaudlitz M., Janka H. T., Steinmetz M., 1998, ApJ, 500, 95

Vogelsberger M., Genel S., Sijacki D., Torrey P., Springel V., Hernquist L., 2013, MNRAS, 436, 3031

Vogelsberger M. et al., 2014a, MNRAS, 444, 1518

Vogelsberger M. et al., 2014b, Nature, 509, 177

Walch S., Naab T., 2015, MNRAS, 451, 2757

Walch S. K., Whitworth A. P., Bisbas T., Wünsch R., Hubber D., 2012, MNRAS, 427, 625

Zhang D., Davis S. W., 2017, ApJ, 839, 54

APPENDIX A: H₂ THERMOCHEMISTRY

As a test for our H_2 thermochemistry, we perform a Strömgren sphere test in a molecular medium (Nickerson et al. 2018, section 3.4). We start with a completely molecular solar-metallicity gas at a density of $n_H = 10^{-3}$ cm^{-3} and a temperature of 13.56×10^3 K. The simulation box has a side of length 15 kpc which is resolved by 32^3 resolution elements. We do not include any photoheating or cooling effects. The central ionization source is an O star which emits radiation spectrum equivalent to a blackbody with an effective temperature of 4.3×10^4 K. Three frequency bins used in this test are the Lyman–Werner (LW; H_2 dissociation) band (11.2–13.6 eV), hydrogen ionization band (13.6–15.2 eV), and H I and H_2 ionization band (15.2–24.6 eV). The total luminosity is set such that the number of H_2 dissociation photons $\dot{N}_{H_2} = 3 \times 10^{48}$ s^{-1} and the number of H I ionization photons is $\dot{N}_{H I} = 5 \times 10^{48}$ s^{-1}. The H_2 ionization rates are taken from Baczynski, Glover & Klessen (2015) and the H_2 dissociation rates and the self-shielding prescriptions are obtained from Nickerson et al. (2018). For these conditions the radius of the Strömgren sphere is

$$r_{s,H I} = \left(\frac{3\dot{N}_{H I}}{4\pi \alpha_{H I} n_H^2} \right)^{1/3} \sim 4.1 \text{ kpc} , \qquad (A1)$$

where $\alpha_{H I}$ is the Case B recombination rate.

Fig. A1 shows the fractional ionization profiles of molecular (blue curve), neutral (red curve) and ionized (green curve) hydrogen after 500 Myr of evolution. The H II region ends sharply at 4.1 kpc as expected. The self-shielding prescription is able to block most of the LW photons from entering into the molecular layer producing a relatively sharp and thin H I layer between the fully ionized H II and fully molecular H_2 layers. This nicely matches with the results obtained by Nickerson et al. (2018), thereby confirming the accuracy of our scheme.
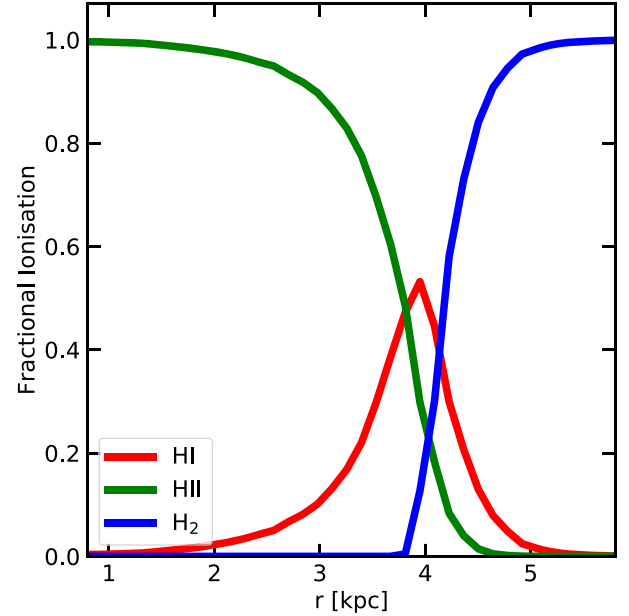

Figure A1. Profiles of the neutral hydrogen (red curve), ionized hydrogen (green curve), and molecular hydrogen (blue curve) fractions as a function of radius around an O star at the end of the molecular Strömgren sphere test.

This paper has been typeset from a TₑX/LATₑX file prepared by the author.